PREPRINT

Title: Harnessing prefrontal-hippocampal theta synchrony to enhance memory-guided choice

Authors: J. J. Stout[1], A. E. George[2], S. Kim[1], H. L. Hallock[3], A. L. Griffin[1,4,*]

[1]Department of Psychological and Brain Sciences, University of Delaware, Newark, DE 19716, USA

[2]Stony Brook University, NY 11794, USA

[3]Neuroscience Program, Lafayette College, Easton, PA 18042, USA

[4]Lead Contact

*Correspondence: amygriff@udel.edu

Abstract

Working memory is correlated with prefrontal-hippocampal oscillatory synchrony, but whether endogenous patterns of synchronized brain rhythms can be used to bias future choice remains unknown. Here, we developed a brain machine interface that detected states of strong and weak theta synchrony for task and neural manipulation. States of strong prefrontal-hippocampal theta coherence were characterized by strengthened prefrontal theta rhythms and were used to enhance memory-guided choice. In follow up experiments and analyses, we show that strong prefrontal-hippocampal theta coherence was associated with task engagement, phase modulation of prefrontal neurons to ventral midline thalamic theta, and heightened excitability in a select group of neurons. Through optogenetic manipulation of the ventral midline thalamus, we produced prefrontal theta rhythms and enhanced prefrontal-hippocampal oscillatory synchrony. These experiments show that prefrontal-hippocampal oscillatory synchrony can be used to bias memory-guided choices and provide evidence in support of the communication through coherence hypothesis.

Introduction

Working memory, the ability to temporarily maintain and mentally manipulate information, is fundamental to cognition (Baddeley, 1986). This ability is known to require communication and neuronal processing across distributed brain regions and is conserved over mammalia (Goldman-Rakic, 1991; Sarnthein et al., 1998; Lee and Kesner, 2003; Winter and Stich, 2005; Wang and Cai, 2006; Eichenbaum, 2008; Fell and Axmacher, 2011; Christophel et al., 2017; Eichenbaum, 2017; Churchwell and Kesner, 2011; Spellman et al., 2015; Hallock et al., 2016; Ito et al., 2015; Bolkan et al., 2017; Ito et al., 2018; Maisson et al., 2018; Lugtmeijer et al., 2021). Cross-brain interactions are thought to be supported by proper timing of action potentials (spikes), and brain rhythms are thought to act as a clocking mechanism (Buzsaki, 2006). Oscillatory activity exists over a range of frequencies, with various frequency bands correlating to neuronal activity (Fries, 2005; Buzsaki, 2006; Fell and Axmacher, 2011; Fries, 2015; Colgin, 2011; Fernández-Ruiz et al 2021). For example, hippocampal rhythms are tightly coupled to the organization of hippocampal neuronal activity patterns in rats (O'Keefe and Recce, 1993), bats (Eliav et al., 2018), primates (Jutras et al., 2009), and humans (Qasim et al., 2021), although the exact frequency can vary over mammalia. The hypothesis that brain rhythms coordinate brain communication by synchronizing neuronal activity is called "communication through coherence" (Fries, 2005; Buzsaki, 2006; Fell and Axmacher, 2011; Fries, 2015).

Disruptions to working memory naturally interfere with a multitude of daily activities and are seen in various disorders such as schizophrenia (Goldman-Rakic, 1994), attention deficit hyperactive disorder (Klingberg et al., 2002), autism spectrum disorders (Kercood et al., 2014), and addiction (Rochat and Khazaal, 2019). While there exist cognitive/behavioral therapeutic interventions for working memory impairments (Klingberg et al., 2002; Rochat and Khazaal, 2019), there remains a critical need to develop new therapeutic approaches. Based on the finding that cross-brain synchronization is correlated with memory (Sarnthein et al., 1998; Kopp et al., 2006; Payne and Kounios, 2009; Anderson et al., 2010), a recent study used transcranial direct alternating current stimulation (tDACS) to rescue age-related working memory deficits in humans by inducing frontal-temporal oscillatory synchrony (Reinhart et al., 2019). Therefore, it is possible that endogenous patterns of neuronal correlation, such as oscillatory synchrony, can be used to enhance working memory and improve therapeutic success.

In rats, decades of research have shown that computations within, and communication between, the medial prefrontal cortex (mPFC) and hippocampus are required for spatial working memory (Dudchenko, 2001; Lee and Kesner, 2003; Wang and Cai, 2006; Horst and Laubach, 2009; Churchwell and Kesner, 2011; Hallock et al., 2013a). Bidirectional communication between the mPFC and dorsal hippocampus is thought to be mediated by the ventral midline thalamus (VMT) given its bidirectional anatomical connections to both brain regions (Vertes, 2002; McKenna and Vertes, 2004; Gabbot et al., 2005; Vertes et al., 2006; Hoover and Vertes, 2007; Hoover and Vertes, 2012; Dolleman-van der Weel et al., 2019; Griffin, 2021), its involvement in spatial working memory (Hembrook and Mair, 2011; Hallock et al., 2013a; Layfield et al., 2015; Hallock et al., 2016), and its role in coordinating mPFC-hippocampal neural synchronization during choice (Hallock et al., 2016; Stout et al., 2022).

Recording studies specifically implicate theta synchrony as a mechanism for mPFC-hippocampal communication. For example, mPFC-hippocampal theta coherence was shown to be stronger prior to correct choices when compared to forced navigation and choice errors (Jones and Wilson, 2005), is stronger when memory is used to guide choice (Sigurdsson et al., 2010; O'Neill et al., 2013; Hallock et al., 2016), and is correlated with rule learning (Benchenane et al., 2010) and task engagement (Guise and Shapiro, 2017). Importantly, at the level of action potential discharge, mPFC neurons phase lock to hippocampal theta rhythms (Siapas et al., 2004; Hyman et al., 2010), and this entrainment is stronger when memory is used to guide choices (Jones and Wilson, 2005; Benchenane et al., 2010; Hallock et al., 2016; Guise and Shapiro, 2017).

These studies raise the possibility that patterns of neural synchronization, like those found between the mPFC and hippocampus, could be used to bias behavior. Consistent with this logic, work from Stephen Berry's lab (Griffin et al., 2004) showed that hippocampal-dependent learning could be facilitated by presenting stimuli during

theta-dominant states. By examining whether spatial working memory dependent choices can be modulated by timing trial initiations to coincide with mPFC-hippocampal theta coupling, we can 1) test gain-of-function mechanisms of synchrony and 2) provide experimental evidence that synchronized neuronal activity leads to, rather than simply correlates with specific choice outcomes.

Here, we developed a brain machine interface to test whether the strength of theta coupling within the mPFC-hippocampal network impacts future choices by leveraging the well-established finding that mPFC-hippocampal theta coherence is stronger when rats perform accurately on spatial memory tasks compared to when they perform poorly (Jones and Wilson, 2005; Hallock et al., 2016). Through follow-up analyses and optogenetic manipulation, we then identify candidate mechanisms by which heightened mPFC-hippocampal theta synchrony supports successful decision-making, pointing to a specific role of VMT in the coordination of mPFC neural activity. This report implicates a promising role for oscillatory synchrony in therapeutic approaches for improving cognitive dysfunction and significantly advances our understanding of how mPFC-hippocampal neural coupling is linked to memory-guided choices.

Results

Development of a closed-loop brain machine interface for coherence-dependent task manipulation

Rats were implanted with stainless steel wires targeting the prelimbic and infralimbic subregions of the medial prefrontal cortex (mPFC) and CA1 of dorsal hippocampus (**Extended Fig. 1**) to record local field potentials (LFPs). To support brain machine interfacing, we designed two independent loops, one processing the neural data in real-time and the other controlling the automatic maze (**Extended Fig. 2**). These loops were then embedded, such that in between maze control, the data analysis loop was implemented (**Fig. 1A**).

Prior to experimentation, we designed our data analysis loop. By iteratively extracting signals into MATLAB from our acquisition system at systematically-increasing lags (25ms-300ms), we found that waiting 250ms before extracting new signals provided reliable streaming between the brain and MATLAB (**Extended Fig. 3A-C**). We then tested the impact of dataset sizes on the strength and the shape of the coherence distribution within the 4-12Hz theta range, in real-time. By linearly increasing the amount of data being analyzed, and calculating coherence over 50 separate intervals from an example rat in real-time, we noticed that the dataset sizes strongly impacted the shape of the coherence distribution (**Extended Fig. 3E-F**) although the effect on coherence magnitude was less robust (**Extended Fig. 3D**). Since the strongest theta frequency (4-12Hz) plateaued at ~8Hz when analyzing dataset sizes of 1.25s (**Extended Fig. 3E**),

we used 1.25s dataset sizes with 250ms steps forward in time (**Extended Fig. 3G**). This approach led to clear transitions between high and low magnitude theta coherence (**Extended Fig. 3H**) indicating that we were accurately tracking coherence in real-time.

Since brain machine interfacing handles data acquired in real-time, we z-score transformed real-time detrended signals against a mean and standard deviation acquired during a 10 minute recording session. We excluded epochs if >1% of the LFP signals were saturated with voltages exceeding 4 standard deviations. Since movement related artifacts often coincided with strong delta (1-4Hz) power (**Extended Fig. 3I**), we also excluded epochs if delta coherence was stronger than theta coherence. When combined, these approaches isolated coherence distributions with clear theta synchrony (6-11Hz; **Fig. 1B**) and high consistency across rats (**Extended Fig. 3I**).

Once these algorithms were defined (**Extended Figs 2-4**), we then trained rats to perform a delayed alternation task until they performed at 70% for two consecutive days. On this spatial working memory task, rats were rewarded for alternating between left and right reward zones, and were sequestered at the base of the maze before each choice (delay phase; **Fig. 1A**). This task was validated to tax working memory by measuring the impact of delay duration on choice outcome. Consistent with the use of delayed-response tasks across species (Dudchenko, 2001; Goldman-Rakic, 1991; Eichenbaum, 2008), longer delay durations led to worse task performance (**Extended Fig. 5A**)

During these training sessions, thousands of theta coherence values were calculated during the delay phases, and distributions of mean theta coherence estimates were created (**Extended Fig. 3J**). Using these distributions, we defined “low” or “weak” theta coherence as 1std below the mean, and “high” or “strong” theta coherence as 1 std above the mean of all theta coherence values. Therefore, each rat had their own unique numerical value defining states of strong and weak theta coherence, which we could then use to control the automated maze (**Fig. 1A**; **Extended Fig. 4**).

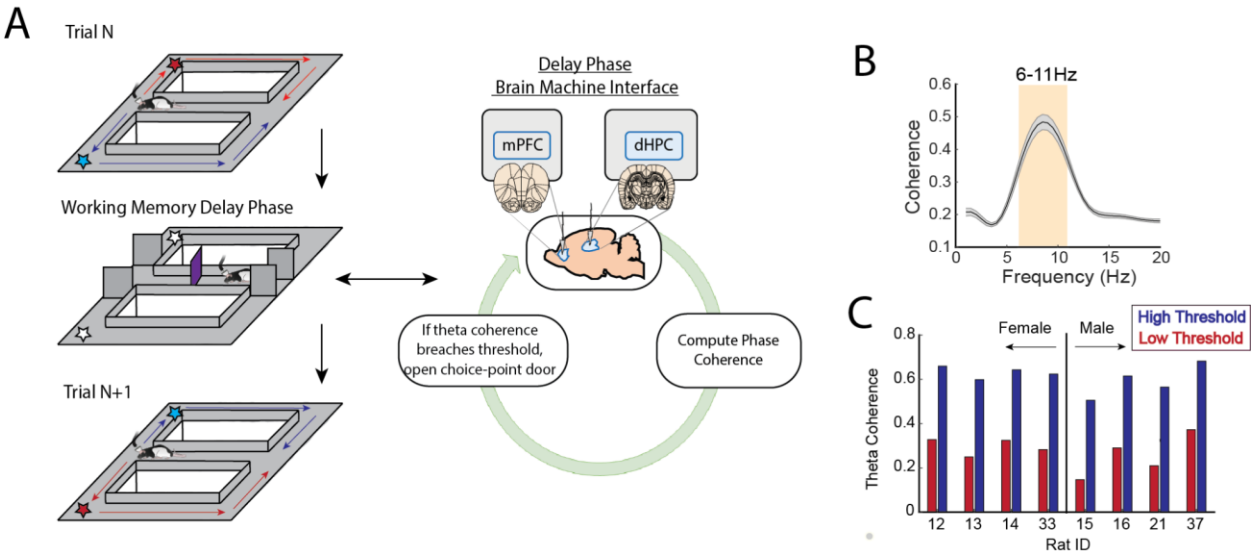

Figure 1 | A brain machine interface that harnesses endogenous mPFC-hippocampal theta coherence on a working memory task.

A) Schematic of brain machine interfacing as rats performed a delayed alternation task on an automated T-maze. The delayed alternation task requires rats to alternate between left and right rewards. Blue arrows and stars denote correct (rewarded) trajectories while red arrows and stars represent incorrect (unrewarded) trajectories. The rat was confined to the delay zone with three barriers (delay phase). On a subset of delay phases, we computed mPFC-hippocampal theta coherence in real-time and trials were initiated contingent upon theta coherence magnitude. **B)** Frequency by coherence distribution calculated on data collected in real-time (N = 8 rats; 4 female, 4 male). For brain machine interfacing experiments, “theta coherence” was defined as the averaged coherence values between 6-11Hz. Data are represented as the mean +/- s.e.m. **C)** Thresholds for high and low magnitude coherence were estimated based on distributions of theta coherence values that were unique to individual rats (see **Extended Fig. 3J** and methods). N = 8 rats (4 female, 4 male).

Initiation of trials during strong mPFC-hippocampal theta coherence improves choice accuracy on a spatial working memory task

Based on multiple reports, mPFC-hippocampal theta coherence is positively correlated with memory-guided decision making (Jones and Wilson, 2005; Benchenane et al., 2010; Hallock et al., 2016). But can theta coherence be used to bias choice behaviors before they occur? To test this idea, we implemented our algorithms described above with an automatic maze to control trial initiations. During

experimentation, our brain machine interface was activated as rats occupied the delay zone and rats were presented with various trial-types within a given session as follows. A small proportion of trials were initiated when mPFC-hippocampal theta coherence was strong (~10%) or weak (~10%) (**Fig. 2A and 2B**). Since increasing delay durations lead to worse task performance (**Extended Fig. 5A**), rats also experienced trials that were yoked to high and low coherence trials via identical delay durations. For example, if trial N were a high coherence trial, our algorithm would log the duration spent in the delay zone to be presented back to the rat within a 10 trial block. These yoked trials were initiated dependent on delay length rather than strength of theta coherence (**Fig. 2C**), meaning that by comparing coherence trials to yoked trials, we minimize the effect of working memory load to test whether coherence state can bias choice.

We predicted that rats would perform better when trials were presented during states of strong mPFC-hippocampal theta coherence relative to yoked controls, and that rats would perform worse when trials were presented during states of weak mPFC-hippocampal theta coherence. Consistent with our first prediction, presenting trials during elevated states of prefrontal-hippocampal theta coherence led to improved choice accuracy (**Fig. 2D**). However, presentation of trials during states of low mPFC-hippocampal theta coherence did not impact task performance relative to yoked controls.

We then examined various measurements of overt behavior to test if behaviors differed between coherence triggered trials and yoked trials. First, we examined the amount of time spent until rats made a choice, defined as the amount of time from the point at which a trial is initiated until rats passed the infrared beam that triggers the reward dispenser (**Extended Fig. 2**). While we found no difference in time-to-choice between high coherence trials and yoked trials, there was a trending difference between low and yoked trials (**Extended Fig. 5B**). Using an analysis to test head-movement complexity (IdPhi; Papale et al., 2012; Redish, 2016), we found no differences between high coherence trials and yoked trials, but did observe less head-movement complexity on low coherence trials relative to yoked (**Extended Fig. 5C**). Next, we analyzed total distance traveled in the epoch used to trigger trials during high and low coherence states (last 1.25s before trial initiation). Since the amount of time was always consistent (1.25s), this approach is a proxy for speed, an indirect correlate of theta (Kropff et al., 2021). We found no differences in movement behavior between coherence trials and yoked trials (**Extended Fig. 5D**). Finally, we found that rats spent similar amounts of time in the delay zone during high and low coherence trials (**Extended Fig. 5E**). These analyses show that high coherence trials could be used to promote correct choices in the absence of clear changes to behavior, indicating that mPFC-hippocampal theta coherence may play a causal role on memory-guided choice.

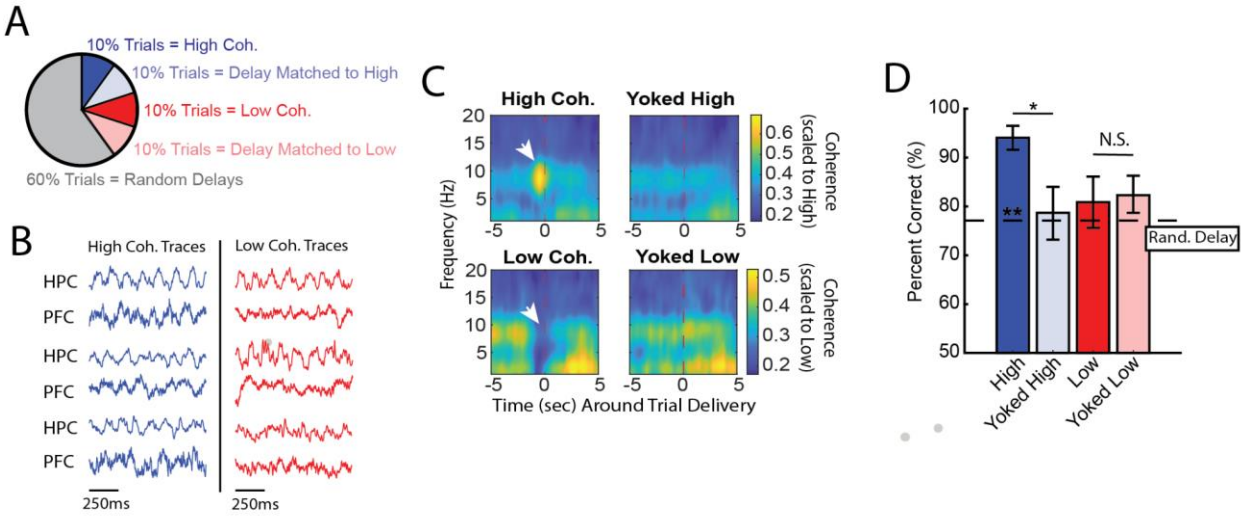

Figure 2 | High mPFC-hippocampal theta coherence can be used to enhance performance of a working memory dependent task

A) Distribution of trial-types within a session. Within 10-trial blocks , 20% of trials were initiated based on high or low mPFC-hippocampal theta coherence, 20% of trials were yoked to the high/low coherence trials, and 60% were triggered following a random delay (5-30s). Yoked trials were identical in delay duration as high/low coherence trials, but triggered independent of coherence magnitude to control for the negative correlation between delay length and task performance (**Extended Fig. 5A**). **B)** Example LFP traces recorded during high and low coherence trials from three representative rats. The mPFC and hippocampal signals were used to compute theta coherence in real-time. **C)** Coherograms representing time around trial initiation (x-axis), coherence frequency (y-axis) and coherence magnitude, with warmer colors indicating higher coherence values. White arrows denote strong (top panel) and weak (bottom panel) theta coherence, as expected on trials triggered during high and low coherence states. Notice that on yoked trials, coherence was rather consistent before and after trial initiation, as expected for trials triggered independent of coherence magnitude. **D)** Relative to yoked trials, presenting choices to rats when mPFC-hippocampal theta coherence was high led to improved task performance ($t(7) = 2.85$, ci = [2.6 to 28.3], $p_{p.c.} = 0.0248$). Trials contingent upon low magnitude theta coherence did not impact task performance compared to delay matched controls ($t(7) = -0.26$, $p_{p.c.} = 0.80$; paired t-test). Follow-up statistical testing revealed that only high coherence trials were significantly greater than performance on random delays, consistent with our planned comparisons between high and yoked trials ($t(7) = 6.12$; $p_{(x4)} = 0.002$). * $p<0.05$, ** $p<0.01$. Colored stars (**) above dashed lines denote significance as measured from comparisons relative to random delay choice outcomes (black) and relative to 70% criterion (gray). Subscript “P.C.” indicates planned comparisons. Subscript “(x4)” indicates unplanned comparisons with Bonferroni corrected p-values for the number of unplanned tests performed.

Prominent prefrontal theta rhythms and heightened pre-choice synchrony characterize high prefrontal-hippocampal theta coherence trials

We then performed offline data analysis to understand the neural dynamics occurring during the high coherence states that improved spatial working memory task performance. Relative to low coherence states, mPFC theta rhythms (6-9Hz) were stronger during high coherence states (**Fig. 3A-3B;** see **Fig. 2B** for example LFP traces). Hippocampal theta rhythms only exhibited a modest elevation in theta power relative to low coherence states. With respect to theta frequency, both mPFC and hippocampal theta rhythms were shifted toward higher frequencies during high coherence states relative to low coherence states, with mPFC theta rhythms approaching 7Hz and hippocampal rhythms approaching 8Hz (**Fig. 3C**). We then analyzed whether these signals exhibited evidence of directionality, the ability for one signal to predict another signal as measured via Granger Causality (Cohen, 2014). Relative to low coherence states, high coherence states were characterized by increased hippocampal-to-mPFC theta directionality (**Fig. 3D**). Thus, the high theta coherence states used to trigger spatial working memory trials were characterized by strong mPFC theta rhythms and hippocampal-to-mPFC theta directionality.

Even though the delay zone was physically close to the choice point (~30cm), we wondered whether high mPFC-hippocampal theta coherence trials impacted synchronization during choice. Therefore, we defined choice-point entry as the infrared beam break immediately preceding the choice (**Extended Fig. 2**). On average, rats took ~1.5-2s to reach this infrared beam from trial initiation, with no significant differences observed between high and low coherence trials (**Fig. 3E**). Thus, we extracted LFPs from -2s to +0.5s surrounding choice-entry (**Fig. 3E**), and calculated coherence over time and frequency (**Fig. 3F**). A normalized difference score was calculated from the resultant coherograms (high-low/high+low), revealing a clear difference in theta coherence magnitude between high and low coherence trials as rats approached the choice (**Fig. 3G**). As expected, high coherence trials showed significantly stronger synchronization at -2s, an approximate for trial initiation (**Fig. 3H**). Interestingly, after the 2s time-point, theta coherence between high and low coherence trials became more similar, but once again differed at ~0.5s pre-choice (**Fig. 3H**). This latter result shows that high mPFC-hippocampal theta coherence trials lead to heightened, pre-choice theta synchrony.

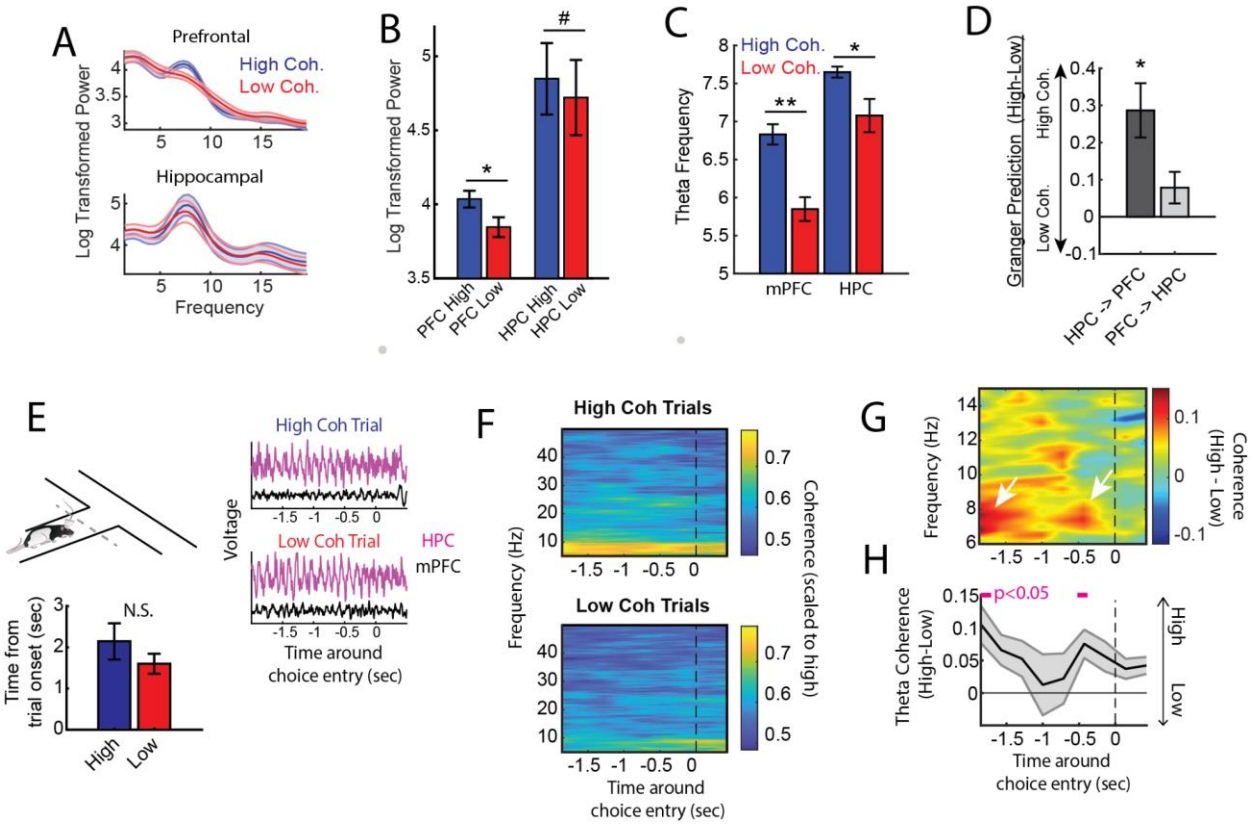

Figure 3 | High mPFC-hippocampal theta coherence trials are gated by prefrontal theta rhythms and lead to heightened pre-choice synchrony

A) Prefrontal and hippocampal power spectra during the high and low coherence epochs used for brain machine interfacing in experiment #1 (**Fig. 1 and 2**). **B)** Prefrontal theta power (6-9Hz) was significantly greater during high coherence epochs ($t(7) = 3.66$, ci = 0.067 to 0.312, $p_{adj(x2)} = 0.016$). Hippocampal theta power was trending in significance ($t(7) = 2.36$, ci = -0.0003 to 0.254, $p = 0.05$). **C)** The frequency (speed) of prefrontal and hippocampal theta oscillations was significantly higher during high coherence states relative to low coherence states (PFC: $t(7) = 5.35$, $p_{adj(x2)} = 0.002$, ci = 0.55 to 1.42; HPC: $t(7) = 3.34$, $p_{adj(x2)} = 0.025$, ci = 0.17 to 0.98). Theta frequency was measured by identifying the frequency corresponding to maximum theta (4-12Hz) power. **D)** Hippocampal-to-prefrontal theta directionality was significantly stronger during high theta coherence states relative to low theta coherence states ($t(7) = 3.9$, ci = [0.11 to 0.46], $p_{adj(x3)} = 0.018$). No significant effect was observed in the prefrontal-hippocampal direction ($t(7) = 1.8$, $p = 0.11$), nor when we compared HPC->PFC vs PFC->HPC ($t(7) = 2.6$, $p_{adj(x3)} = 0.1$). Data are represented as the mean +/- s.e.m. across 8 rats. *p<0.05, **p<0.01, paired t-tests with Bonferroni p-value corrections when p<0.05. Difference scores were tested against a null of 0. **E)** LFP signals (jittered for visualization) were extracted from 2s before choice point entry (as defined by infrared beam breaks) and 0.5s afterwards. Bar graphs show that the average time to choice-entry for high coherence and low coherence trials was between 1.5-2s. **F)** Averaged

coherograms (N = 8 rats) showing coherence as a function of frequency and time surrounding choice point entry. **G)** Difference of the coherograms shown in **F**. White arrows point to initial 6-9Hz synchronization at -2s which approximates trial onset (see bar graph in **E**), and a second time point of heightened theta synchrony before choice entry. **H)** Normalized difference scores representing theta coherence as a function of time. Theta coherence at choice-entry was significantly stronger on trials triggered by high coherence relative to trials triggered during low coherence (*-2s from choice entry:* $t(7) = 3.7$; $p_{adj}=0.043$; *-0.5s from choice entry:* $t(7) = 3.46$; $p_{adj}=0.043$). Magenta lines denote $p<0.05$ after Benjaminin Hochberg corrections.

Prefrontal-hippocampal theta coherence states are linked to task engagement

Our findings thus far indicate that high coherence states could be used to enhance spatial working memory task performance seconds before the actual decision. If mPFC-hippocampal theta coherence reflects attention to internal variables held in working memory, a potential correlate of Baddeley's *central executive* (Baddeley, 1986), then we would expect instances of theta coherence to emerge more frequently as rats prepare for an upcoming choice, corroborating the work by Guise and Shapiro (2017). Consistent with this idea, on spatial working memory tasks with predictable and fixed delay intervals, our lab has anecdotally observed that rats tend to exhibit orienting behaviors toward the maze barricade that confines them to the start box. These behaviors are especially prominent near the end of the delay. We therefore predicted that high coherence states would become more frequent in well-trained animals as the upcoming trial nears.

To test this prediction, we examined the evolution of theta coherence across a predictable delay interval on two different spatial working memory tasks from 6 well-trained rats (N = 44 sessions; **Fig. 4A**)**.** We calculated theta coherence in 1.25s windows, every 250ms (**Fig. 4B;** see **Extended Fig. 3G-H**). Unlike our experiments and analyses described above, we did not exclude signals if delta rhythms were stronger in magnitude than theta rhythms in order to capture the entire coherence distribution over time. By splitting the delay intervals in halves, we calculated the probability of observing high coherence events (# of high coherence events/number of epochs). Consistent with our prediction, we discovered that high coherence states became more frequent towards the end of a fixed and predictable delay interval (**Fig. 4C;** see **Extended Fig. 6** for coherence thresholds and session counts) and correspondingly, low coherence events became less frequent (**Fig. 4D**). This finding suggests that strong theta coherence states reflect task engagement, and combined with our brain machine interfacing experiments, supports the claim that mPFC-hippocampal theta coherence is optimal for spatial working memory in rats.

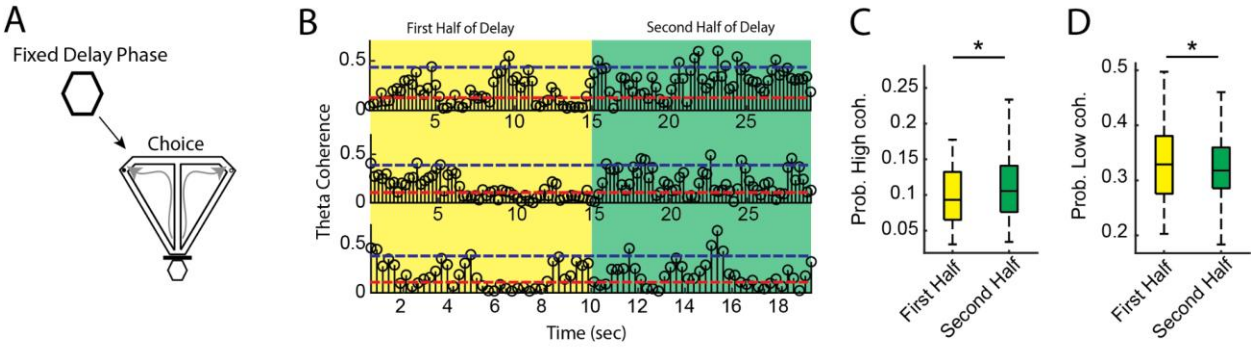

Figure 4 | The frequency of high mPFC-hippocampal theta coherence states were modulated by a fixed delay duration

A) Well-trained rats (N = 44 sessions from 6 male rats) performed two spatial working memory tasks with fixed delay durations of either 30s or 20s (see methods). **B)** Coherence was calculated in 1.25s epochs, shifted 250ms forward in time over the duration of the delay interval. Like **Fig. 1C**, high and low coherence thresholds were derived. Yellow backdrop indicates the first half of the delay while green backdrop indicates the second half of the delay from 3 representative trials (two different tasks; one task had 30s delays, the other task had 20s delays). **C)** The probability of high coherence events (# coherence events > coherence threshold / # coherence events) was significantly greater during the second half of the delay relative to the first half of the delay ($Z = -2.57$, $p = 0.01$). **D)** Likewise, low coherence events were less common during the second half of the delay relative to the first half ($Z = 2.12$, $p = 0.03$; Signrank test). Data are represented as boxplots with median (solid line), and the 25th and 75th percentiles. *p<0.05.

Prefrontal-thalamic theta rhythms couple during high mPFC-hippocampal theta coherence states

What are the mechanisms supporting strong mPFC-hippocampal theta synchrony? While the ventral hippocampus sends a direct projection to the mPFC that has been demonstrated to be is important for mPFC-dorsal hippocampal theta coherence (O'Neill et al., 2013), the mPFC does not send a return projection (Sesack et al., 1989; Jay and Witter, 1991; Gabbot et al., 2005; Hoover and Vertes, 2007). One promising route for bidirectional neural interactions is through the ventral midline thalamus (VMT). Previous work demonstrated that inactivating the VMT disrupts the performance on spatial working memory tasks (Layfield et al., 2015; Hallock et al., 2016; Maisson et al., 2018), and reduces mPFC-hippocampal theta synchrony, predominantly during choice (Hallock et al., 2016) and pausing and reorienting behaviors (Stout et al., 2022) thought to reflect deliberation (Redish, 2016). Given that thalamic output projections provide a means for glutamatergic excitation to both the mPFC and hippocampus (Dolleman-van der Weel et al., 2019), we next wondered how

neural interactions varied across the mPFC-thalamo-hippocampal network with coherence state.

To probe this question, we examined datasets with simultaneous mPFC, VMT, and dorsal hippocampus recordings from 3 rats performing a spatial working memory task (N = 22 sessions; **Fig. 5A; Extended Fig. 6B;** Hallock et al., 2016; Stout and Griffin, 2020). We extracted neural data as rats occupied the delay zone, then defined and detected epochs of strong and weak mPFC-hippocampal theta coherence offline (**Fig. 5B**; **Extended Fig. 6A**). Corroborating the findings from our brain machine interfacing experiment (**Figs 2 and 3**), high theta coherence states were characterized by strong 6-9Hz theta rhythms in the mPFC (**Figs 5C and 5D**). Intriguingly, the magnitude change of theta power between high and low coherence states was strongest in the mPFC, followed by the VMT, then the hippocampus (**Fig. 5D**), which we suspect is attributed to the power of hippocampal theta rhythms relative to those in mPFC and VMT (**Fig. 5C**).

Relative to low coherence epochs, the mPFC was differentially and simultaneously synchronized to the VMT and hippocampus during high coherence states (**Fig. 5E**). Moreover, high coherence states were characterized by a stronger change in neural synchronization between the mPFC and VMT, relative to the VMT and hippocampus (**Fig. 5F**). Thus, while VMT and hippocampal theta rhythms were present during low coherence states, high coherence states were characterized by strengthened mPFC theta rhythms and strengthened connectivity across the mPFC-thalamo-hippocampal network.

To then understand how the VMT statistically modulates the mPFC and hippocampus, and in turn, how the VMT is modulated by these regions, we performed multivariate grange prediction. By focusing on separate unidirectional pathways (e.g. hippocampus-to-VMT-to-mPFC and mPFC-to-VMT-to-hippocampus pathways), we compared granger prediction estimates averaged within the theta (6-9Hz) range between high and low coherence epochs. In the hippocampus-to-VMT-to-mPFC direction, we found that both the VMT and the hippocampus predicted mPFC theta rhythms (**Fig. 5G**). Then in the mPFC-to-VMT-to-hippocampus direction, we found the mPFC to predict both VMT and hippocampal rhythms (**Fig. 5H**). Interestingly, we did not find high coherence states to be characterized by differential directionality between the VMT and hippocampus. Taken together, when the mPFC and hippocampus were strongly coupled at theta, mPFC-thalamic interactions were strengthened.

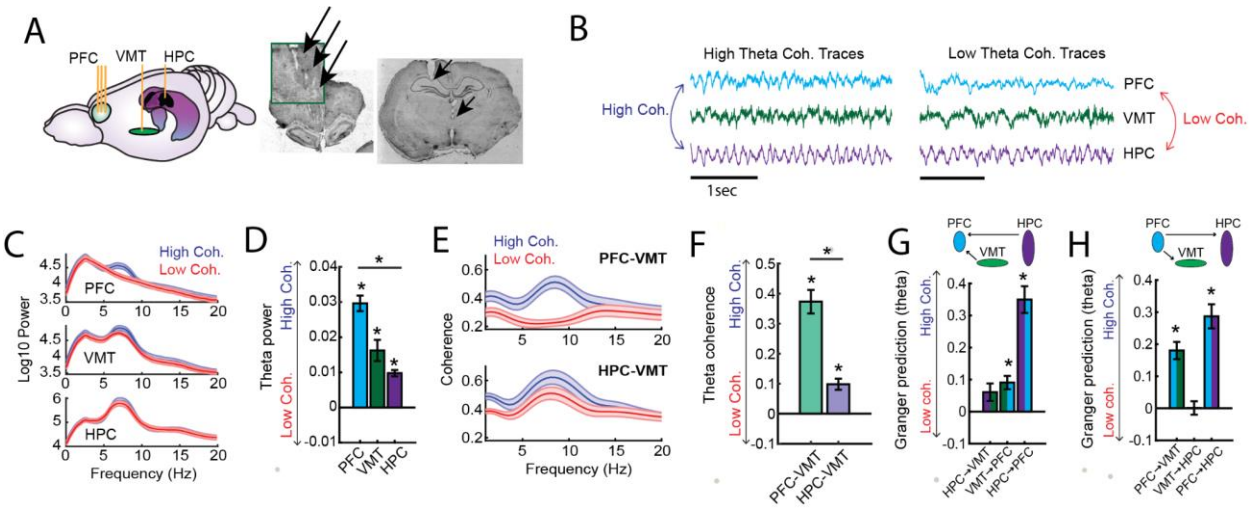

Figure 5 | Coupling of prefrontal-thalamo-hippocampal theta rhythms are modulated by mPFC-hippocampal theta coherence state

A) Neural data were recorded from the mPFC, ventral midline thalamus (VMT), and hippocampal of 3 rats (N = 22 sessions). *Right panel* shows triple site recordings taken from a representative rat. Green box shows example tetrode tracks from the mPFC. **B)** High and low coherence epochs (1.25s epochs) were identified during the delay phase of a spatial working memory task and LFPs from the ventral midline thalamus were extracted accordingly. For visualization purposes, the data shown are collapsed across high or low coherence epochs. **C)** Frequency by coherence plots from the mPFC (top panel), VMT (middle panel), and hippocampus (bottom panel). Compare these data to (**Fig. 3**). **D)** Normalized difference scores comparing theta (6-9Hz) power between high and low coherence epochs. There was a main effect of brain region on the coherence difference score ($F(2,65) = 20.8$; $p < 0.001$; one-way ANOVA) with each brain area showing higher theta power during high coherence states relative to low coherence states (PFC: $t(21) = 13.36$, ci = 0.025 to 0.034, $p < 0.001$; VMT: $t(21) = 5.4$, ci = 0.01 to 0.02, $p < 0.001$; HPC: $t(21) = 10.7$, ci = 0.008 to 0.01, $p < 0.001$). **E)** Frequency by coherence plots showing strong coupling between the mPFC and VMT during high coherence states relative to low coherence states. **F)** Relative to low coherence states, mPFC-VMT and HPC-VMT theta coherence was stronger during high coherence states and mPFC-VMT synchrony changed significantly more than VMT-HPC synchrony (mPFC-VMT: $t(21) = 9.52$, ci = 0.29 to 0.45, $p < 0.001$; VMT-HPC: $t(21) = 5.3$, ci = 0.06 to 0.14, $p < 0.001$; t-test against 0-null; mPFC-VMT vs VMT-HPC: $t(21) = 5.77$, ci = 0.18 to 0.37, $p < 0.001$; paired t-test). **G)** Mutivariate granger prediction estimates at theta (6-9Hz) were represented as a normalized difference score (High - Low coherence states). In the hippocampus-VMT-mPFC direction, both VMT and hippocampus predicted mPFC theta rhythms more strongly during high coherence states relative to low coherence states (VMT-mPFC: $t(21) = 4.37$, ci = 0.05 to 0.13, $p < 0.001$; hippocampus-mPFC: $t(21) = 8.4$, ci = 0.26 to 0.44, $p < 0.001$). **H)** In the mPFC-VMT-hippocampal direction, the mPFC predicted VMT theta and the mPFC predicted hippocampal theta more strongly

on high coherence states relative to low coherence states (mPFC-VMT: $t(21) = 6.7$, ci = 0.12 to 0.24, $p < 0.001$; mPFC-hippocampus: $t(21) = 7.57$, ci = 0.21 to 0.37, $p < 0.001$; t-test against 0-null). *$p<0.001$

Prefrontal spiking is modulated by theta oscillations across the prefrontal-thalamo-hippocampal network

According to the communication through coherence hypothesis, rhythmic coordination of neural activity patterns facilitates communication across brain regions through the synchronous waxing and waning of excitation and inhibition (Buzsaki, 2006; Fries, 2015). When populations of neurons are simultaneously active during states of excitation, they are thought to coordinate downstream neuronal activity (Buzsaki, 2006) and undergo synaptic plasticity (Fries, 2015). During high mPFC-hippocampal theta coherence states, pyramidal neurons and interneurons are tuned to hippocampal theta rhythms form cell assemblies (Benchenane et al., 2010). Thus, we suspect that states of strong mPFC-hippocampal theta coherence enhanced spatial working memory task performance (**Fig. 2**) by coordinating action potential discharging across the brain, like we observed with brain rhythm synchronization (**Fig. 5**). Specifically, we predicted to find mPFC neurons that synchronized to both VMT and hippocampal theta rhythms in a manner dependent on the strength of mPFC-hippocampal theta synchrony.

We identified high and low coherence events, then included spikes belonging uniquely to those states (**Fig. 6A**). Spikes and their corresponding LFP phases were then extracted and phase-locking was estimated via Rayleigh's test for non-uniformity (**Fig. 6B** shows an example mPFC unit modulated by VMT theta during high coherence states). Out of 276 putative pyramidal neurons, 94 met criteria for inclusion (see methods) with simultaneous mPFC and hippocampal LFPs, while 46 met inclusion criterion with simultaneous mPFC, VMT, and hippocampal LFPs. 11.7% of all neurons were modulated by hippocampal theta, 11.7% by mPFC theta (largely separate populations from those modulated by hippocampal theta), and 6.5% by VMT theta. During high coherence states, 7.4% of mPFC neurons phase locked to their local theta rhythm, while 4.2% of neurons phase locked during low coherence states. Relative to VMT theta rhythms, 4.3% of neurons phase locked to theta during high coherence states, while 2.2% of neurons phase locked to theta during low coherence states. Finally, while there were equal numbers of neurons phase locked to hippocampal theta during high and low coherence states (6.4%; **Fig. 6C**), these populations were largely unique (**Fig. 6C** pie chart). Therefore, relative to low coherence states, high mPFC-hippocampal theta coherence states were characterized by increased mPFC phase locking the local and thalamic theta rhythms, and a unique population of neurons modulated by hippocampal theta.

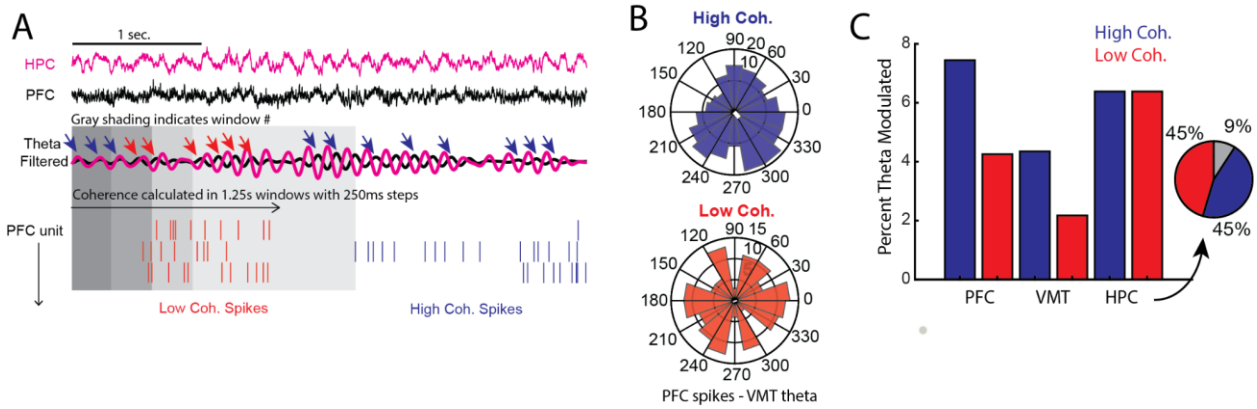

Figure 6 | High prefrontal-hippocampal theta coherence states modulate prefrontal-thalamo spike-phase coupling

A) High and low coherence epochs were identified using a windowing approach (1.25s with 250ms steps) as described in methods, then spiking data across simultaneously recorded mPFC putative pyramidal neurons were extracted. *Top panel* shows raw mPFC and hippocampal LFP signals. *Middle panel* shows theta filtered signals overlaid. The gray boxes represent the moving window analysis, where coherence was calculated in discrete epochs and spiking data (*bottom panel*) were extracted if they uniquely occurred during low or high coherence epochs. Red arrows point to inconsistent phase relationships, while blue arrows show rather consistent phase relationships. *Bottom panel,* spike raster plots show whether spiking occurred uniquely during high (blue) or low (red) coherence epochs. Spikes overlapping with high and low coherence states were excluded. **B)** Polar plots from a representative mPFC neuron that entrained more significantly to VMT theta during high mPFC-hippocampal theta coherence states relative to low coherence states (High Coherence: Z = 3.6, p = 0.03; Low Coherence: Z = 0.08, p = 0.9). Histogram represents the distribution of spike-phase values. Mean result length vector is shown as a white bar in the center. **C)** Percentage of significantly modulated mPFC units to mPFC theta, VMT theta, and hippocampal theta. Notice similar levels of entrainment to hippocampal theta on high and low coherence trials (compare to **Fig. 3A and Fig. 5C**), but greater numbers of units modulated by local mPFC and thalamic rhythms on high compared to low coherence states. Pie chart shows distribution of mPFC neurons phase locked to hippocampal theta. Blue shading indicates percentage of neurons modulated during high coherence states, red shading indicates percentage of neurons modulated by low coherence states, and gray shading shows percentage of neurons modulated during both.

A small population of prefrontal neurons show heightened excitability during high prefrontal-hippocampal theta coherence states

Given the increased frequency of mPFC units modulated by thalamic and hippocampal oscillations during high theta coherence states (**Fig. 6**), we next explored the impact of theta coherence state on neuronal firing rates. We extracted spike counts from high and low coherence states across all 276 neurons and calculated firing rates, which account for differences in the number of high and low coherence events. Neurons were then excluded if their trial-averaged firing rates were 0, leaving us with 234 neurons. Consistent with entrainment analysis, a rather small population (~5%; 12/234) of units showed rate modulation by theta coherence magnitude (**Fig. 7A**). Interestingly, of that population, a majority (75%) showed higher firing activity during high theta coherence states relative to low theta coherence states, indicating heightened neuronal excitability amongst a select group of neurons.

We then wondered if the magnitude of mPFC-hippocampal theta synchrony impacted neuronal representation. Therefore, we extracted spike-rates as rats performed a spatial working memory task, then compared firing activity between left and right choices as rats navigated along the central stem and engaged in choice (**Fig. 7B**; N = 3 rats on a delayed alternation task, N = 3 rats on a delayed non-match to position task). A two-way ANOVA was performed on each unit to measure the effect of stem position and turn direction on firing rate activity. Of the neurons modulated by theta coherence during the delay phase, 25% (3/12 units) showed task modulation (**Fig. 7C**). With respect to the entire population of neurons (234), 29% were modulated by the task (stem position or turn direction), meaning that a similar number of neurons were modulated by task demands regardless of theta coherence modulation (**Fig. 7D**). Thus, while high theta coherence states tend to activate mPFC neurons, the distribution of these neurons coding for future task variables is no different from the rest of the population.

Since firing rate activity during the delay phase is thought to be related to working memory dependent choices in primates (Goldman-Rakic, 1994) and rodents (Bolkan et al., 2017), we wondered whether those neurons activated by theta coherence state also coded for task variables. To test this idea, we extracted delay-phase firing rates and tested whether these neurons were modulated by future turn direction (**Fig. 7E**). Of the 12 neurons modulated by coherence, only 1 (8%) engaged in firing rate modulation by coherence state (**Fig. 7F**). Relative to the entire population, 6% of neurons were modulated by future choice during the delay phase (**Fig. 7G**), indicating that high theta coherence states activated a select group of neurons irrespective of their involvement in task representation.

In summary, we found that relative to low theta coherence states, high theta coherence states activate a greater proportion of mPFC neurons during the memory-dependent delay period. While this rate modulation did not translate to greater task coding, we propose these findings to indicate that high theta synchronization states, which were used to bias future choices and were characterized by heightened neural synchrony across the mPFC-thalamo-hippocampal network, also promotes excitability in a highly specific neuronal population.

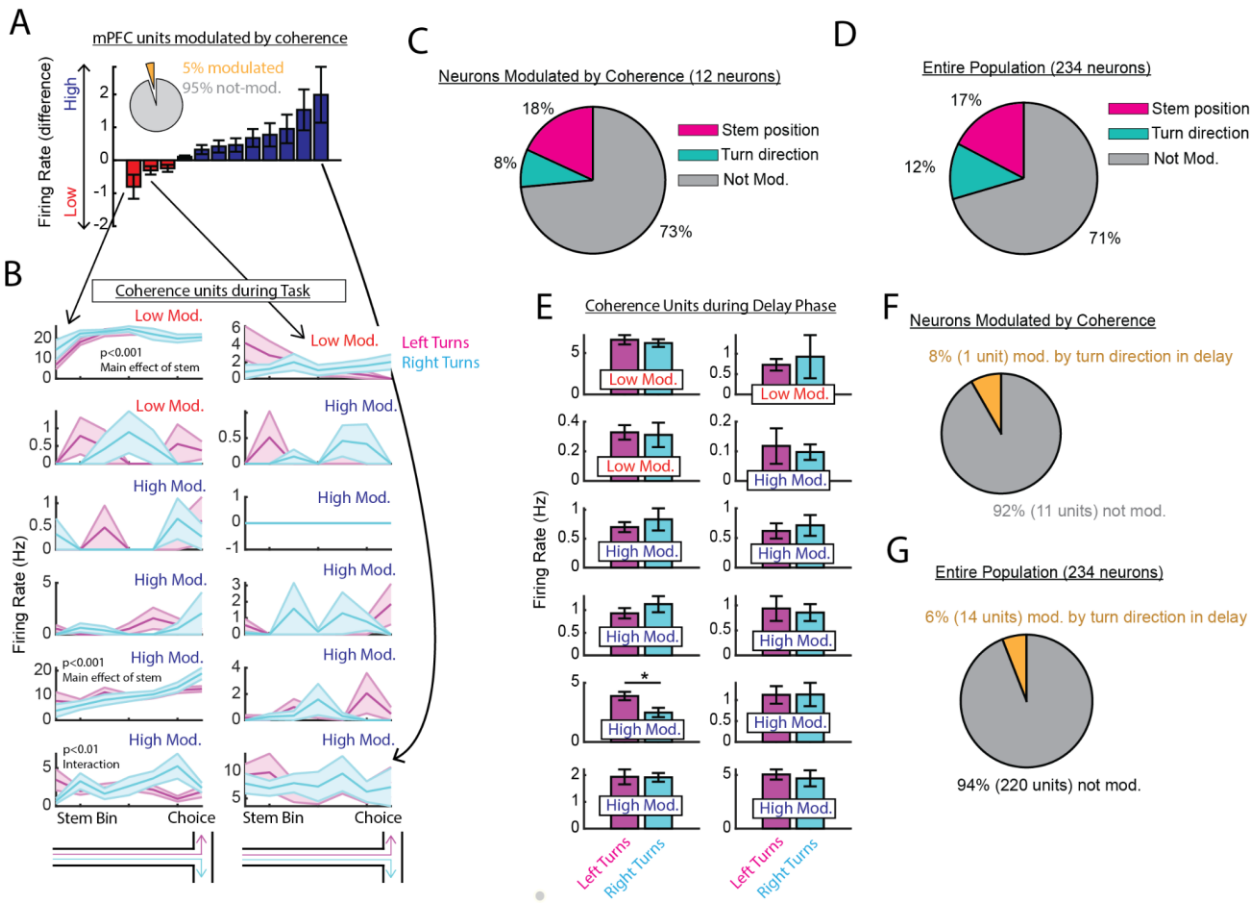

Figure 7 | The effect of mPFC-hippocampal theta coherence magnitude on mPFC firing rates

A) Pie chart represents the percentage of significantly modulated units by the magnitude of theta coherence. Bar graph represents those 5% of modulated units as a difference score (firing rate during high coherence - firing rate during low coherence). These units were then sorted by magnitude of firing rate difference. Notice that a majority of the modulated units showed heightened excitability during high coherence states. **B)** Example firing rates from neurons in **(A)** as rats engaged in a spatial working memory task. X-axis represents the stem (6 bins), and the choice point (1 bin). Magenta

colors denote left turns, cyan color denotes right turns. Data were analyzed with a two-way ANOVA. **C)** Percentage of neurons modulated by position on the stem, or turn direction are shown in pink and teal, respectively. **D)** Percentage of modulated units from all recorded mPFC neurons. **E)** Firing rates were calculated during the delay and organized by whether a future choice was left or right. **F)** Pie chart demonstrated percentage of modulated units from the data seen in **(E)**. **G)** Pie chart representing unit delay phase firing rates modulated by future choice for the entire population of mPFC neurons. Data are represented as the mean ± s.e.m. *p<0.05 t-test. ANOVA statistics shown in figure panels.

Optogenetic activation of the VMT dynamically regulates prefrontal-hippocampal theta rhythms

Previous research showed that inactivation of the VMT drastically reduced mPFC firing rates and disrupted mPFC-hippocampal theta synchrony only during choice processes (Hallock et al., 2016). Since VMT inactivation only reduced mPFC-hippocampal theta coherence during choice, these data indicate that the VMT may coordinate neural synchronization during selective brain states. To test the hypothesis that the VMT is sufficient to produce mPFC-hippocampal theta coherence, we injected the VMT with AAV5-hSyn-ChR2-eYPF to create and embed channelrhodopsin2 at the membrane of VMT neurons, a proton pump that promotes excitation of neurons with blue light stimulation. After 4-6 weeks of recovery and viral incubation, we pulsed a blue laser at 7-8Hz (2s on 2-8s off) targeting the VMT while recording from the mPFC (N = 3 rats) and the hippocampus (N = 2 rats; **Fig. 8A**). As a within-subject control, we also stimulated the VMT with a red laser to account for any effects of tissue heating. Stimulation of red and blue lasers were randomly interleaved within a recording session.

Optogenetic stimulation of the VMT between 7-8Hz produced a large negative deflection in the mPFC voltage and enhanced mPFC theta rhythms across all rats (**Fig. 8B-D**). Upon initial analysis, we noticed a large reduction in mPFC-hippocampal theta coherence (**Extended Figs 7A-D**), which led us to visually inspect the raw and theta filtered signals. While there existed variability across trials, we noticed that upon VMT stimulation, some trials showed an initial desynchronization of mPFC-hippocampal theta rhythms, followed by synchrony (**Fig. 8C and D**). Since we also noticed mPFC theta to taper-off in magnitude after a few seconds, we focused our analysis on 0.5s-1.5s from stimulation. We found that optogenetic activation of VMT increased mPFC theta rhythms, enhanced mPFC-hippocampal theta synchrony, but minimally impacted hippocampal theta (**Figs. 8C and 8D**).

In closing, VMT stimulation readily and robustly enhanced mPFC theta rhythms, and could desynchronize (**Extended Fig. 7**) or synchronize (**Fig. 8**) mPFC-hippocampal theta oscillations. Given the profound effect of VMT stimulation on mPFC theta, and because mPFC theta rhythms were stronger during endogenously observed high mPFC-hippocampal theta coherence states (**Figs. 3 and 5**), we propose that the VMT

dynamically regulates mPFC oscillations to support synchrony. It is important to note that we did not account for the phase of hippocampal theta oscillations during VMT stimulation, which likely contributed to the variable effects on synchrony. As a future direction, controlling for the phase of hippocampal theta rhythms during VMT stimulation may more significantly enhance theta synchrony. Nonetheless, these data show that the VMT can readily influence prefrontal theta rhythms, minimally impacts hippocampal rhythms, and is capable of modulating theta coherence.

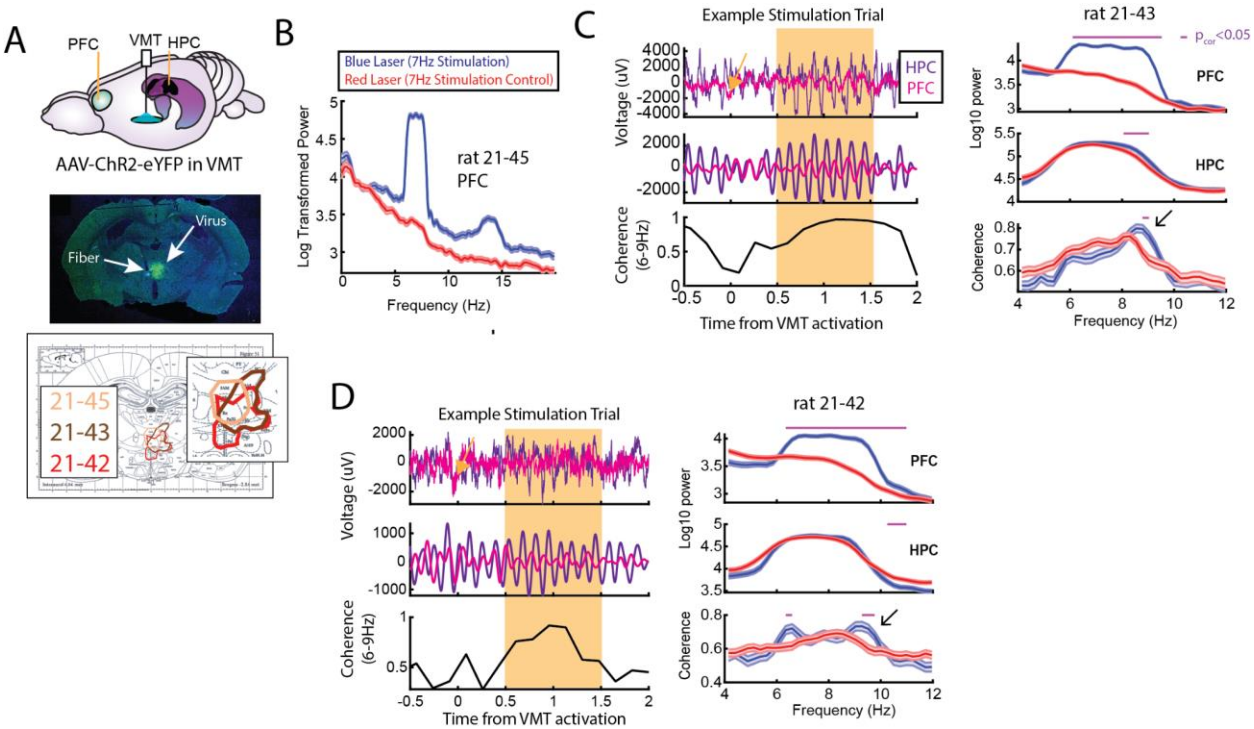

Figure 8 | Optogenetic activation of the ventral midline thalamus produces prefrontal theta and dynamically modulates prefrontal-hippocampal theta coherence

A) *Top panel,* Schematic demonstrating recordings from the mPFC and hippocampus with optogenetic activation of the VMT. *Middle panel*, example histological confirmation of fiber implant and viral expression targeting the VMT. *Bottom panel.* Viral expression at similar viral injection coordinates. Notice that all rats showed overlap in viral expression in the nucleus reuniens (brain section overlay from Paxinos and Watson, 2006). **B)** Optogenetic activation of the VMT at 7Hz produced prefrontal theta rhythms. N = 83 blue laser stimulation events and 88 red laser stimulation events. **C)** *Left panel,* example trial showing the variable effect of VMT stimulation. Notice that in this trial, VMT activation at 7Hz caused a large deflection in the mPFC LFP, followed by coupled theta rhythms. *Right panel*, analysis of power spectral densities and mPFC-

hippocampal theta coherence. Notice that VMT stimulation enhanced theta synchrony in the window shown in the *left panel* (N = 113 blue laser stimulation events and 101 red laser stimulation events). **D)** Optogenetic activation of the VMT at 8Hz, dependent on the presence of hippocampal theta rhythms produced highly consistent results from rat 21-43 and 21-45. Namely, VMT stimulation produced prefrontal theta rhythms (consistent with 21-45 and 21-43) and boosted theta coherence in the timing demarcated by the yellow box in the *left panel* (consistent with 21-43). N = 64 blue laser stimulation events and 104 red laser stimulation events. Data are represented as the mean ± s.e.m. Magenta bars denote $p<0.05$ by means of a Rank-sum test and following Benjamini Hochberg corrections.

Discussion

Consistent with the hypothesis that synchronized neural activity between brain regions supports cognition (Fries, 2005; Buzsaki, 2006; Fries, 2015), we discovered that endogenous mPFC-hippocampal theta synchrony could be harnessed to improve the performance of a spatial working memory task. High coherence trials were characterized by strong mPFC theta rhythms, heightened hippocampal-to-mPFC theta directionality, and greater pre-choice theta synchrony relative to low coherence trials. In follow up experiments and analyses, we show that coupling of mPFC and hippocampal theta rhythms were modulated by the structure of the delay phase and were linked to strengthened mPFC-thalamic synchrony at the level of brain rhythms and mPFC action potential discharging. Through optogenetic manipulations, we show that the VMT is capable of regulating mPFC theta rhythms and mPFC-hippocampal theta synchrony. These results point to oscillatory synchrony as a promising means for therapeutic intervention in cognitive dysfunction and emphasize prefrontal-thalamic interactions when prefrontal and hippocampal theta rhythms are coupled.

The communication through coherence hypothesis posits that through synchronized waxing and waning of excitability, there exists coherent temporal windows for the coordination of action potential discharging across the brain (Fries, 2015). Consistent with this hypothesis, we used states of strong mPFC-hippocampal theta coherence to enhance the performance of a spatial working memory task, and found that these states were characterized by strengthened interactions between the mPFC and ventral midline thalamus at the level of LFP and spikes.

While volume conduction contributes to LFP (Kajikawa and Schroeder, 2011), it is unlikely that a volume conducted signal from the hippocampus drove our results because 1) we observed strong hippocampal theta rhythms during low coherence states, and 2) our brain machine interfacing LFPs were referenced to an electrode placed in cerebellum, which should have also have been contaminated by volume conduction. While we found a surprisingly small number of mPFC neurons with phase and rate modulations to theta coherence magnitude, these findings can be explained in part by our analysis. Since we filtered spikes for high and low theta coherence events,

with low coherence events showing prominent theta (**Figs 3 and 5**), we did not account for running speed or LFP-state (theta vs large irregular amplitude activity) like past work (Siapas et al., 2005; Jones and Wilson, 2005; Hallock et al., 2016; Zielinski et al., 2019; Tang, Shin et al., 2021). Including this latter criterion is important, but became impractical for analyzing this dataset due to multiple thresholds of spike elimination (see methods). Future studies should record large and simultaneous ensembles across the mPFC-thalamo-hippocampal network, and monitor the data for instances of high and low theta coherence in multiple, long-duration recording sessions.

Since mPFC-hippocampal theta coherence was used to enhance task performance, we sought to characterize potential mechanisms supporting this effect. The manner by which these areas interact is thought to be supported through multiple pathways. One route is via direct hippocampal-to-prefrontal projections (Sesack et al., 1989; Jay and Witter, 1991; Spellman et al., 2015), and another route through the VMT (Vertes, 2002; McKenna and Vertes, 2004; Vertes et al., 2006; Hoover and Vertes, 2012; Dolleman-van der Weel, 2019; Griffin, 2021). Unlike the unidirectional projection arising from the hippocampus, the VMT is bidirectionally connected with both the hippocampus and mPFC. Previous research from our lab showed that VMT inactivation disrupted working memory (Layfield et al., 2015; Hallock et al., 2013b; Hallock et al., 2016; Maisson et al., 2018), choice-dependent mPFC-hippocampal theta coherence, mPFC phase locking to hippocampal rhythms, and abolished mPFC firing activity (Hallock et al., 2016). Given the decades of research showing that mPFC-hippocampal synchronization is linked to memory-guided choice, these data indicate that the VMT was required for choice-dependent mPFC-hippocampal interactions. Based on our findings, we add that this thalamic nucleus is capable of strengthening or decoupling mPFC-hippocampal synchrony, and that these states of strong mPFC-hippocampal synchrony were characterized by heightened mPFC-thalamic interactions. Given the homogeneity of glutamatergic neurons in the thalamus, a thalamically derived theta in the cortex must be indirect, in that there is some other theta driver to the thalamus. Some candidate theta drivers are the hippocampus, supramammillary nucleus (Ito et al., 2018), or the medial/lateral septum (Hoover and Vertes, 2007; Schlecht et al., 2022). Since the strength of hippocampal theta was only slightly stronger during high theta coherence states compared to low theta coherence states (**Figs. 3 and 5**), we question whether this endogenous change in hippocampal theta was sufficient to produce mPFC theta. Moreover, inactivation of the supramammillary nucleus primarily disrupted thalamo-hippocampal interactions, with minimal impacts on mPFC theta and mPFC representations (Ito et al., 2018). Future research should examine the circuit level mechanisms supporting thalamic and mPFC theta coordination.

Clinically, our findings provide a promising avenue to rescue cognitive deficits in humans. Consistent with our work, a recent study found that inducing states of theta synchrony between frontal and temporal regions via transcranial alternating-current stimulation, rescued age related memory impairments (Reinhart et al., 2019). Our findings suggest that tapping into pre-existing neural dynamics also holds significant

promise for improving memory. We hypothesize that non-invasive stimulation techniques prior to therapy, paired with synchrony-dependent working memory practice via brain machine interfacing, could pose a viable intervention to improve working memory deficits. In closing, the use of brain machine interfacing holds significant promise for clinical and neuroscientific advance.

References

Anderson, K. L., Rajagovindan, R., Ghacibeh, G. A., Meador, K. J., & Ding, M. (2010). Theta oscillations mediate interaction between prefrontal cortex and medial temporal lobe in human memory. Cerebral cortex, 20(7), 1604-1612.

Baddeley, A. (1986). Working Memory. Oxford: Oxford University Press.

Barnett, L., & Seth, A. K. (2014). The MVGC multivariate Granger causality toolbox: a new approach to Granger-causal inference. Journal of neuroscience methods, 223, 50-68.

Benchenane, K., Peyrache, A., Khamassi, M., Tierney, P. L., Gioanni, Y., Battaglia, F. P., & Wiener, S. I. (2010). Coherent theta oscillations and reorganization of spike timing in the hippocampal-prefrontal network upon learning. Neuron, 66(6), 921-936.

Bolkan, S. S., Stujenske, J. M., Parnaudeau, S., Spellman, T. J., Rauffenbart, C., Abbas, A. I., ... & Kellendonk, C. (2017). Thalamic projections sustain prefrontal activity during working memory maintenance. Nature neuroscience, 20(7), 987-996.

Buzsaki, G. (2006). Rhythms of the Brain. Oxford university press.

Christophel, T. B., Klink, P. C., Spitzer, B., Roelfsema, P. R., & Haynes, J. D. (2017). The distributed nature of working memory. Trends in cognitive sciences, 21(2), 111-124.

Churchwell, J. C., & Kesner, R. P. (2011). Hippocampal-prefrontal dynamics in spatial working memory: interactions and independent parallel processing. Behavioural brain research, 225(2), 389-395.

Cohen, M. X. (2014). Analyzing neural time series data: theory and practice. MIT press.

Cohen, M. X. (2017). MATLAB for brain and cognitive scientists. MIT Press.

Colgin, L. L. (2011). Oscillations and hippocampal–prefrontal synchrony. Current opinion in neurobiology, 21(3), 467-474.

Dolleman-van der Weel, M. J., Griffin, A. L., Ito, H. T., Shapiro, M. L., Witter, M. P., Vertes, R. P., & Allen, T. A. (2019). The nucleus reuniens of the thalamus sits at the nexus of a hippocampus and medial prefrontal cortex circuit enabling memory and behavior. Learning & Memory, 26(7), 191-205.

Dudchenko, P. A. (2001). How do animals actually solve the T maze?. Behavioral neuroscience, 115(4), 850.

Eichenbaum, H. (2008). Learning & memory (p. 494). New York: WW Norton & Company.

Eichenbaum, H. (2017). Prefrontal–hippocampal interactions in episodic memory. Nature Reviews Neuroscience, 18(9), 547-558.

Eliav, T., Geva-Sagiv, M., Yartsev, M. M., Finkelstein, A., Rubin, A., Las, L., & Ulanovsky, N. (2018). Nonoscillatory phase coding and synchronization in the bat hippocampal formation. Cell, 175(4), 1119-1130.

Fell, J., & Axmacher, N. (2011). The role of phase synchronization in memory processes. Nature reviews neuroscience, 12(2), 105-118.

Fernández-Ruiz, A., Oliva, A., Soula, M., Rocha-Almeida, F., Nagy, G. A., Martin-Vazquez, G., & Buzsáki, G. (2021). Gamma rhythm communication between entorhinal cortex and dentate gyrus neuronal assemblies. Science, 372(6537), eabf3119.

Fries, P. (2005). A mechanism for cognitive dynamics: neuronal communication through neuronal coherence. Trends in cognitive sciences, 9(10), 474-480.

Fries, P. (2015). Rhythms for cognition: communication through coherence. Neuron, 88(1), 220-235.

Gabbott, P. L., Warner, T. A., Jays, P. R., Salway, P., & Busby, S. J. (2005). Prefrontal cortex in the rat: projections to subcortical autonomic, motor, and limbic centers. Journal of Comparative Neurology, 492(2), 145-177.

Goldman-Rakic, P. S. (1991). Cellular and circuit basis of working memory in prefrontal cortex of nonhuman primates. Progress in brain research, 85, 325-336.

Goldman-Rakic, P. S. (1994). Working memory dysfunction in schizophrenia.

Griffin, A. L. (2021). The nucleus reuniens orchestrates prefrontal-hippocampal synchrony during spatial working memory. Neuroscience & Biobehavioral Reviews, 128, 415-420.

Griffin, A. L., Asaka, Y., Darling, R. D., & Berry, S. D. (2004). Theta-contingent trial presentation accelerates learning rate and enhances hippocampal plasticity during trace eyeblink conditioning. Behavioral neuroscience, 118(2), 403.

Guise, K. G., & Shapiro, M. L. (2017). Medial prefrontal cortex reduces memory interference by modifying hippocampal encoding. Neuron, 94(1), 183-192.

Hallock, H. L., Arreola, A. C., Shaw, C. L., & Griffin, A. L. (2013a). Dissociable roles of the dorsal striatum and dorsal hippocampus in conditional discrimination and spatial alternation T-maze tasks. Neurobiology of learning and memory, 100, 108-116.

Hallock, H. L., Wang, A., Shaw, C. L., & Griffin, A. L. (2013b). Transient inactivation of the thalamic nucleus reuniens and rhomboid nucleus produces deficits of a working-memory dependent tactile-visual conditional discrimination task. Behavioral neuroscience, 127(6), 860.

Hallock, H. L., Wang, A., & Griffin, A. L. (2016). Ventral midline thalamus is critical for hippocampal–prefrontal synchrony and spatial working memory. Journal of Neuroscience, 36(32), 8372-8389.

Hembrook, J. R., & Mair, R. G. (2011). Lesions of reuniens and rhomboid thalamic nuclei impair radial maze win- shift performance. Hippocampus, 21(8), 815-826.

Hoover, W. B., & Vertes, R. P. (2007). Anatomical analysis of afferent projections to the medial prefrontal cortex in the rat. Brain Structure and Function, 212, 149-179.

Hoover, W. B., & Vertes, R. P. (2012). Collateral projections from nucleus reuniens of thalamus to hippocampus and medial prefrontal cortex in the rat: a single and double retrograde fluorescent labeling study. Brain Structure and Function, 217, 191-209.

Horst, N. K., & Laubach, M. (2009). The role of rat dorsomedial prefrontal cortex in spatial working memory. Neuroscience, 164(2), 444-456.

Hyman, J. M., Zilli, E. A., Paley, A. M., & Hasselmo, M. E. (2010). Working memory performance correlates with prefrontal-hippocampal theta interactions but not with prefrontal neuron firing rates. Frontiers in integrative neuroscience, 2.

Ito, H. T., Moser, E. I., & Moser, M. B. (2018). Supramammillary nucleus modulates spike-time coordination in the prefrontal-thalamo-hippocampal circuit during navigation. Neuron, 99(3), 576-587.

Ito, H. T., Zhang, S. J., Witter, M. P., Moser, E. I., & Moser, M. B. (2015). A prefrontal–thalamo–hippocampal circuit for goal-directed spatial navigation. Nature, 522(7554), 50-55.

Janabi-Sharifi, F., Hayward, V., & Chen, C. S. (2000). Discrete-time adaptive windowing for velocity estimation. IEEE Transactions on control systems technology, 8(6), 1003-1009.

Jay, T. M., & Witter, M. P. (1991). Distribution of hippocampal CA1 and subicular efferents in the prefrontal cortex of the rat studied by means of anterograde transport of Phaseolus vulgaris-leucoagglutinin. Journal of Comparative Neurology, 313(4), 574-586.

Jones, M. W., & Wilson, M. A. (2005). Theta rhythms coordinate hippocampal–prefrontal interactions in a spatial memory task. PLoS biology, 3(12), e402.

Jutras, M. J., Fries, P., & Buffalo, E. A. (2009). Gamma-band synchronization in the macaque hippocampus and memory formation. Journal of Neuroscience, 29(40), 12521-12531.

Kajikawa, Y., & Schroeder, C. E. (2011). How local is the local field potential?. Neuron, 72(5), 847-858.

Kercood, S., Grskovic, J. A., Banda, D., & Begeske, J. (2014). Working memory and autism: A review of literature. Research in autism spectrum disorders, 8(10), 1316-1332.

Klingberg, T., Forssberg, H., & Westerberg, H. (2002). Training of working memory in children with ADHD. Journal of clinical and experimental neuropsychology, 24(6), 781-791.

Kopp, F., Schröger, E., & Lipka, S. (2006). Synchronized brain activity during rehearsal and short-term memory disruption by irrelevant speech is affected by recall mode. International Journal of Psychophysiology, 61(2), 188-203.

Kropff, E., Carmichael, J. E., Moser, E. I., & Moser, M. B. (2021). Frequency of theta rhythm is controlled by acceleration, but not speed, in running rats. Neuron, 109(6), 1029-1039.

Layfield, D. M., Patel, M., Hallock, H., & Griffin, A. L. (2015). Inactivation of the nucleus reuniens/rhomboid causes a delay-dependent impairment of spatial working memory. Neurobiology of learning and memory, 125, 163-167.

Lee, I., & Kesner, R. P. (2003). Time-dependent relationship between the dorsal hippocampus and the prefrontal cortex in spatial memory. Journal of Neuroscience, 23(4), 1517-1523.

Lugtmeijer, S., Geerligs, L., De Leeuw, F. E., De Haan, E. H., & Kessels, R. P. (2021). Are visual working memory and episodic memory distinct processes? Insight from stroke patients by lesion-symptom mapping. Brain Structure and Function, 226(6), 1713-1726.

Maisson, D. J. N., Gemzik, Z. M., & Griffin, A. L. (2018). Optogenetic suppression of the nucleus reuniens selectively impairs encoding during spatial working memory. Neurobiology of Learning and Memory, 155, 78-85.

McKenna, J. T., & Vertes, R. P. (2004). Afferent projections to nucleus reuniens of the thalamus. Journal of comparative neurology, 480(2), 115-142.

Mitra, P. (2007). Observed brain dynamics. Oxford University Press.

O'Keefe, J., & Recce, M. L. (1993). Phase relationship between hippocampal place units and the EEG theta rhythm. Hippocampus, 3(3), 317-330.

O'Neill, P. K., Gordon, J. A., & Sigurdsson, T. (2013). Theta oscillations in the medial prefrontal cortex are modulated by spatial working memory and synchronize with the hippocampus through its ventral subregion. Journal of Neuroscience, 33(35), 14211-14224.

Papale, A. E., Stott, J. J., Powell, N. J., Regier, P. S., & Redish, A. D. (2012). Interactions between deliberation and delay-discounting in rats. Cognitive, Affective, & Behavioral Neuroscience, 12(3), 513-526.

Pastalkova, E., Itskov, V., Amarasingham, A., & Buzsaki, G. (2008). Internally generated cell assembly sequences in the rat hippocampus. Science, 321(5894), 1322-1327.

Paxinos, G., & Watson, C. (2006). The rat brain in stereotaxic coordinates: hard cover edition. Elsevier.

Payne, L., & Kounios, J. (2009). Coherent oscillatory networks supporting short-term memory retention. Brain research, 1247, 126-132.

Qasim, S. E., Fried, I., & Jacobs, J. (2021). Phase precession in the human hippocampus and entorhinal cortex. Cell, 184(12), 3242-3255.

Ranck Jr, J. B. (1973). Studies on single neurons in dorsal hippocampal formation and septum in unrestrained rats: Part I. Behavioral correlates and firing repertoires. Experimental neurology, 41(2), 462-531.

Redish, A. D. (2016). Vicarious trial and error. Nature Reviews Neuroscience, 17(3), 147-159.

Reinhart, R. M., & Nguyen, J. A. (2019). Working memory revived in older adults by synchronizing rhythmic brain circuits. Nature neuroscience, 22(5), 820-827.

Rochat, L., & Khazaal, Y. (2019). Cognitive remediation therapy of working memory in addictive disorders: An individualized, tailored, and recovery-oriented approach. Expert review of neurotherapeutics, 19(4), 285-287.

Sarnthein, J., Petsche, H., Rappelsberger, P., Shaw, G. L., & Von Stein, A. (1998). Synchronization between prefrontal and posterior association cortex during human working memory. Proceedings of the National Academy of Sciences, 95(12), 7092-7096.

Schlecht, M., Jayachandran, M., Rasch, G. E., & Allen, T. A. (2022). Dual projecting cells linking thalamic and cortical communication routes between the medial prefrontal cortex and hippocampus. Neurobiology of Learning and Memory, 188, 107586.

Seager, M. A., Johnson, L. D., Chabot, E. S., Asaka, Y., & Berry, S. D. (2002). Oscillatory brain states and learning: Impact of hippocampal theta-contingent training. Proceedings of the national academy of sciences, 99(3), 1616-1620.

Sesack, S. R., Deutch, A. Y., Roth, R. H., & Bunney, B. S. (1989). Topographical organization of the efferent projections of the medial prefrontal cortex in the rat: an anterograde tract- tracing study with Phaseolus vulgaris leucoagglutinin. Journal of Comparative Neurology, 290(2), 213-242.

Siapas, A. G., Lubenov, E. V., & Wilson, M. A. (2005). Prefrontal phase locking to hippocampal theta oscillations. Neuron, 46(1), 141-151.

Sigurdsson, T., Stark, K. L., Karayiorgou, M., Gogos, J. A., & Gordon, J. A. (2010). Impaired hippocampal–prefrontal synchrony in a genetic mouse model of schizophrenia. Nature, 464(7289), 763-767.

Spellman, T., Rigotti, M., Ahmari, S. E., Fusi, S., Gogos, J. A., & Gordon, J. A. (2015). Hippocampal–prefrontal input supports spatial encoding in working memory. Nature, 522(7556), 309-314.

Stout, J. J., & Griffin, A. L. (2020). Representations of on-going behavior and future actions during a spatial working memory task by a high firing-rate population of medial prefrontal cortex neurons. Frontiers in Behavioral Neuroscience, 14, 151.

Stout, J. J., Hallock, H. L., George, A. E., Adiraju, S. S., & Griffin, A. L. (2022). The ventral midline thalamus coordinates prefrontal–hippocampal neural synchrony during vicarious trial and error. Scientific Reports, 12(1), 10940.

Tang, W., Shin, J. D., & Jadhav, S. P. (2021). Multiple time-scales of decision-making in the hippocampus and prefrontal cortex. Elife, 10, e66227.

Vertes, R. P. (2002). Analysis of projections from the medial prefrontal cortex to the thalamus in the rat, with emphasis on nucleus reuniens. Journal of comparative neurology, 442(2), 163-187.

Vertes, R. P., Hoover, W. B., Do Valle, A. C., Sherman, A., & Rodriguez, J. J. (2006). Efferent projections of reuniens and rhomboid nuclei of the thalamus in the rat. Journal of comparative neurology, 499(5), 768-796.

Wang, G. W., & Cai, J. X. (2006). Disconnection of the hippocampal–prefrontal cortical circuits impairs spatial working memory performance in rats. Behavioural brain research, 175(2), 329-336.

Winter, Y., & Stich, K. P. (2005). Foraging in a complex naturalistic environment: capacity of spatial working memory in flower bats. Journal of Experimental Biology, 208(3), 539-548.

Zielinski, M. C., Shin, J. D., & Jadhav, S. P. (2019). Coherent coding of spatial position mediated by theta oscillations in the hippocampus and prefrontal cortex. Journal of Neuroscience, 39(23), 4550-4565.

Acknowledgements

We would like to thank A. Garcia, D. Shaw, A. Cestone, Z. Gemzik, H. Rosenblum, J. Hoopman, E. Walzl, J. Mace, and S. Adiraju for technical assistance. The brain cartoons were created by W. Tang. The rat cartoons were created by G. Costa. Both images were downloaded from SciDraw.io. We would also like to thank Sylvain Le Marchand for capturing images of viral expression for the optogenetics experiments. This work was made possible by the Office of Laboratory Medicine. We thank the staff at Neuralynx for technical support. Research was funded by the National Institute of Mental Health under R21 MH117687.

Data Availability Statement

Source data and the corresponding code to reproduce results will be made freely available with the peer-reviewed publication of this manuscript. A small portion of data for brain machine interfacing parameter decisions were generated using signals detected in real-time and are not available (**Extended Fig. 3**).

Author Contributions

A.L.G proposed the brain machine interfacing experiments. A.L.G., J.J.S., and A.E.G. modified and extended upon the proposed experiments. J.J.S developed the brain machine interfacing methods and wrote the code. J.J.S., A.E.G., and S.K. contributed to data collection. J.J.S. and H.L.H. collected data used from previous publications. J.J.S. analyzed the data. All authors contributed to the writing of this manuscript.

Competing interests

The authors declare no competing interests.

Methods

Subjects

Subjects were 16 adult (>postnatal day 90) Long Evans Hooded rats. For experiment #1 (**Figs 1-3**), there were 4 adult male and 4 adult female rats with simultaneous mPFC and hippocampus local field potential (LFP) recordings. In the analyses from **Figs. 4-7**, there were 6 adult male rats, 3 receiving mPFC-VMT-hippocampus recordings, and 3 receiving mPFC/hippocampus recordings (rats were from Hallock et al., 2016, and Stout and Griffin, 2020). For the optogenetic experiment (**Fig. 8**), 3 male rats received optogenetic virus injections and fiber placement targeting the VMT (2 with simultaneous mPFC/hippocampus recordings and 1 with silicon probe recording from the mPFC). Each rat was placed on mild food restriction (3-4 pellets for females, 4-5 pellets for males) to maintain ~85-90% *ad libitum* body weight. Rats maintained a 12hr light/dark cycle in a humidity controlled colony room. Experimentation was performed during the light cycle (8am-5pm) at approximately the same time each day +/- ~1 hour.

Automated T-maze

The automated maze was in the shape of a figure 8 (**Fig. 1A**) and was purchased from MazeEngineers. The total width of the maze was 136.5cm and the total length was 74.8cm. Floor width corresponded to ~12.7cm, while wall height was ~20.3cm. The delay zone was a rectangular shape, 12.7cm wide and 32.7cm long. Doors were pneumatically controlled via a silent air compressor (SilentAire Super Silent 30-TC), reward delivery (45mg bio-serv chocolate pellets) was controlled through an automated pellet dispenser, and both were under the control of Arduino powered infrared beams (Adafruit) via custom MATLAB programming (**Extended Fig. 2**). Walls were placed on the exterior of the maze with distinct visual cues on the left and right

choice arms. For two rats, interior walls were placed to improve maze running behavior. In the delay zone, the south facing wall was lowered to improve mobility. The maze was surrounded by black curtains with visual cues matching the maze and experimentation occurred in a dimly lit room.

Brain machine interface

The brain machine interface relied upon extracting real-time LFPs, performing coherence analysis, and triggering the choice point door to open according to the magnitude of prefrontal-hippocampal theta coherence. Real time signal extraction was performed using the Neuralynx Netcom v3.1.0 package code (*NlxGetNewCSCData.m*). Since signals were extracted serially, this code was modified in-house (*NlxGetNewCSCData_2signals.m*) and verified by feeding the same recording lead through two separate recorded channels (**Extended Fig. 3C**). Once data were extracted in real time, LFPs were detrended by subtracting a third degree polynomial (*detrend.m*). Next, LFPs were filtered for large amplitude artifacts by z-score transforming the real time signal against the mean and standard deviation of all real time signals obtained from the delay period of delayed alternation training. If 1% of the signal contained voltage fluctuations that exceeded 4std from the mean, the epoch was ignored. Mean squared coherence was calculated on accepted data across a range of frequencies (1:0.5:20) using the *mscohere.m* function, and theta coherence was defined as 6-11Hz synchrony according to the frequency x coherence plot (**Fig. 1B**). Because movement artifacts coincided with high magnitude 1-4Hz (delta) coherence (**Extended Fig. 3I**), signals were filtered a second time and only accepted if theta coherence was greater than delta coherence. In real time, LFPs were extracted in 1.25s windows with 0.25s overlaps (**Extended Fig. 3G-H**). LFP sampling at 250ms intervals prevented acquisition failures (**Extended Fig. 3B**). Calculating coherence over 1.25s windows provided a stable ~8Hz peak in the theta coherence distribution (**Extended Fig. 3E-F**). In practice, sampling windows were ~1.28s with ~280ms overlap and yielded stable coherence estimates across epochs (**Extended Fig. 3G**).

Behavior and experimentation

Rats were handled for 5 days in the experimentation room with the lights on and placed on mild food restriction prior to habituation to the automated T-maze. Habituation consisted of “goal-box” training and “forced-runs” training. For goal-box training, rats were placed near the reward dispensers for 3 minutes and were required to eat all pellets within 90s for 6 trials (3 left dispenser / 3 right dispenser). One rat was excluded after not passing goal box training for 7 consecutive days. For forced-runs, rats traversed the maze to receive a reward at the reward dispenser and were required to eat all rewards for at least 1 day. Rats were often run for multiple forced runs days. In between traversals, rats waited in the delay pedestal. After maze habituation, rats were trained to perform the continuous alternation (CA) task, where choice alternations were

reinforced with chocolate pellets. The CA task was performed 5 days/week for 30min or 40 trials. Rats were required to perform at 80% accuracy for two consecutive days before and after surgery. After surgical recovery, rats were re-handled for 5 days, then placed on the CA task until they again reached criterion. The CA task was implemented to ensure that coherence-contingent choice outcomes (see **Brain machine interface**) were not confounded by alternation rule acquisition. Rats were then exposed to the spatial working memory delayed alternation (DA) task, where in between choice alternations, rats waited in the delay zone for a 5-30s delay period (randomly distributed). Once rats performed the DA task for 2 consecutive days at 70% accuracy, our brain machine interface testing occurred. DA task training was implemented to rule-out any effect of changing environmental demands on the rats (e.g. the introduction of a delay period), as well as to normalize task performance prior to experimentation. During testing, the experimenter was blinded to trial-type and trials were excluded if unexpected events occurred before the choice (e.g. loud noises, fear behavior, twisted recording tether) then saved as a MATLAB variable after the session ended. 20% of trials were experimental (10% high coherence/10% low coherence), while 80% of trials were controls (**Fig. 2A**). Trial-types were presented psuedo-randomly because high and low coherence trials were required to be presented prior to delay matched control trials. Within blocks of 10 trials, 2 were experimental, 2 were delay matched controls, and 6 were random delays. On a given experimental trial, if rats did not breach the coherence threshold, the trial was initiated after 30s, and the delay matched control trial was replaced with a random delay.

With respect to data used from Hallock et al., 2016 (N = 3 rats) and Stout et al., 2020 (N = 3 rats), 6 rats were trained to perform a delayed alternation task or delayed non-match to position task to 80% criterion for two consecutive days. With respect to the delayed alternation task, sessions were included if performance was >75% because these rats switched between performing the delayed alternation task and a striatal-dependent task. Unlike the brain machine interfacing experiment where delays varied between 5 and 30s, rats from Hallock and colleagues (2016) had predictable delay durations of 30s. With respect to the delayed non-match to position task, sessions were included if performance was >80% (Stout and Griffin, 2020). This task differs from delayed alteration in that each trial is comprised of a sample phase, where rats are forced to navigate towards the left or right reward zone, followed by a free choice. Rats were rewarded if their choice was an alternation from the sample phase. Sample phase turn directions were pseudo-randomized to ensure there were no more than 3 same-turn directions in a row. Data were extracted from delay periods, which separated the sample from choice phase and were 20s in duration. From choice to sample, there was an intertrial interval of 40s.

Surgery

Isoflurane (1-4%) anesthetic was used prior to shaving the scalp and placing rats in the stereotaxic instrument (Kopf). Puralube was applied to rats' eyes throughout the surgery. Lidocaine was injected subcutaneously in the scalp, the scalp was sterilized using Chlorhexidine solution (0.2% chlorhexidine gluconate), then incised if rats did not exhibit a kick reflex and eye blink reflex. Bleeding was controlled using hydrogen peroxide. Once the skull was level, bregma was identified, and craniotomies were made above the medial prefrontal cortex (mPFC) and dorsal hippocampus (dHPC). mPFC craniotomies were made at + 3.1mm anterior and +/- 1.0mm lateral to bregma, while dHPC craniotomies were made at -3.7mm posterior and +/- 2.2mm lateral to bregma. Implants were always on the same hemisphere, but hemispheres were decided pseudo-randomly for each rat in a sex matched manner. In practice, 3 right hemisphere (2 female, 1 male) and 5 left hemisphere (2 female, 3 male) implants were successful. 6 rats received cannula implants targeting the contralateral ventral midline thalamus and 1 rat received electrode implants targeting the contralateral striatum for separate experiments that occurred after the data collected in this report. One rat received a 64 channel silicon probe implant (Buzsaki 64L, Neuronexus) at 3.7mm anterior to bregma and 0.7mm lateral. A small burr hole was made over the cerebellum for reference wire implants at -10 to -12mm posterior and +/- ~1.5mm lateral to bregma. 5-6 bone screws (Fine Science Tools) were implanted as support screws, and 1-2 bone screws were implanted over the cerebellum for grounding. LFP implants were mounted to the skull using Metabond and the remainder of the micro-drive was mounted using dental acrylic (Lang Dental). A shield surrounding the electronic interface board was built using a plastic medicine cup or a copper mesh shielding. Copper mesh shielding was grounded to the same screw grounding the electronic interface board. Rats were given a dose of flunixin (Banamine; 2.5 mg/kg) at least 20 minutes prior to removal from anesthesia and were placed on ~15mg Childrens Ibuprofen for a 7-day recovery.

For optogenetic infusions (AAV5-hSyn-ChR2-eYFP) and fiber implants, 21-43 and 21-45 received viral injections at 1.8mm, 2.4mm, and 3mm posterior to bregma. Posterior injections of 2.4mm and 3mm were injected at 2.2mm lateral and 7.1mm ventral to brain surface at a 15 degree angle. The injection at 1.8mm posterior to bregma was injected at 2.2mm lateral to bregma and 6.6mm ventral to brain surface at a 15 degree angle. Once the microsyringe was placed into the brain, it sat for 10 minutes, after which, an injection of .1uL/min was performed for 2.5min at each location. The fiber was placed at 2.4mm posterior to bregma, 2.2mm lateral to bregma, and 6.8mm ventral to brain surface from the opposite hemisphere.

Rat 21-42 received two separate injections at 1.9mm posterior to bregma and 1.95mm lateral to bregma. The microsyringe was placed at 7mm ventral to brain surface, allowed to settle for 10 minutes, after which a 2.5 minute injection took place at .1uL/min. Once the injection was complete, the microsyringe was slowly raised dorsally

to 6.7mm ventral to brain surface, and another injection of 2.5uL occurred. The fiber was then placed at 6.4mm from brain surface from the opposite hemisphere.

Perfusion and histology

Rats were euthanized with a lethal dose of sodium pentobarbital and perfused with PBS and 4% PFA. After ≥ 2 days of post-fixing the implant and brain in 4% PFA, brains were extracted and cryo-protected by submerging the brain in a mixture of 4% PFA and 30% sucrose. After 1-2 weeks, or when brains sunk to the vial floor, brains were sectioned between 30-50um while visually identifying implant locations. Sections were Cresyl stained and imaged using a digital microscope (plugable).

Electrophysiological recordings

LFPs were recorded on a Neuralynx (Digital Lynx) 64 channel recording system. Neuralynx software (Cheetah) was used to sample LFPs at 2kHz, and filter LFPs between 1-600Hz. mPFC LFP implants consisted of two stainless steel wires, while dHPC implants consisted of 4 stainless steel wires, each offset dorso-ventrally by ~0.25-0.5mm. Single units were collected using tetrodes and reported in previous publications (Hallock et al., 2016; Stout and Griffin, 2020). Spikes were sampled at 32kHz, bandpass filtered between 0.6-6kHz, and thresholded at 50-75uV. Clusters were cut using SpikeSort3D with KlustaKwik, then manually curated. Putative pyramidal neurons were selected based on spike waveform and interspike-intervals (Ranck, 1973). For silicon probe recordings, signals were referenced to the ground wire. Each recording lead was then re-referenced offline by removing the common average over all recording sites.

Granger Prediction

All follow-up spectral analyses were performed on data that was inspected for break-through artifacts. Bivariate Granger prediction was used to assess directionality between PFC and HPC LFPs (code from Hallock et al., 2016). Granger prediction is calculated using the variance in errors obtained from univariate and bivariate autoregressions on lagged LFPs. As reported by Cohen (2014):

$$\text{Univariate: } PFC_t = \sum_{n=1}^{k} a_n PFC_{t-n} + e_t$$

$$\text{Bivariate: } PFC_t = \sum_{n=1}^{k} a_n PFC_{t-n} + \sum_{n=1}^{k} b_n HPC_{t-n} + \epsilon_t$$

For each model, *t* reflects the time point for the LFP data, *k* reflects the model order, *n* reflects the lag, *e* represents the variance not explained by a univariate model, while ϵ reflects the variance not explained by the bivariate model. Granger prediction in the HPC-to-PFC direction is estimated as such:

$$GC_{HPC->PFC} = log\left(\frac{Var[e]}{Var[\epsilon]}\right)$$

Spectral estimates are calculated using Geweke's method in both directions (e.g. PFC-to-HPC and HPC-to-PFC). Bayes Information Criterion (BIC) was used to estimate model order for each signal and was defined as the lag providing the smallest BIC value (up to 20 lags). The averaged BIC value across all signals was then rounded and applied to each signal for granger prediction analysis. For multivariate granger prediction analysis, we used the freely available MVGC toolbox (Barnett and Seth, 2014) downloaded from Github. The information criterion and VAR model estimation mode was set to Lowess Regression ('LWR') and BIC was estimated by testing model orders up to 100 lags with an autocovariance lag of 1000. The same BIC value was used for all signals, as described above. Demeaned signals were fit to a VAR model (*tsdata_to_var.m*), the autocovariance sequence was estimated (*var_to_autocov.m*) and the VAR model was checked for potential error, such as violations to stationarity. Finally, the spectral pairwise causality estimations were calculated (*var_to_spwcgc.m*). Granger prediction and model order estimation was performed on signals of identical size (1.25s) for both high and low coherence epochs. Code is available on the labs Github page (*get_mvgc_parameters.m, get_mvgc_modelOrder.m, get_mvgc_freqGranger.m*).

Spectral power

Power spectral densities were estimated using the chronux toolbox (Mitra, 2007) *mtspectrumc* using 3 tapers with a time-bandwidth product of 2 and *pspectrum.m*. To account for the 1/f power law, power spectral estimates were log10 transformed. The frequency corresponding to maximum theta power was defined as "theta frequency" and performed over the 4-12Hz frequency range.

Spike analysis

Boolean spike trains were created by finding spike times that corresponded with LFP times via *dsearchn* from the delay phase of 2 separate spatial working memory tasks. On the delayed alternation task (Hallock et al., 2016), this constituted a 30s delay phase and on the delayed non-match to position task this constituted 20s delay intervals in between sample and choice task phases (Stout and Griffin, 2020). LFPs were concatenated across trials, and slow frequency movement artifacts were removed by filtering the signal between 5 and 100Hz with a third-degree butterworth filter. To further detect candidate artifacts that present as large voltage deflections, data were concatenated over all sessions for each rat, then z-score transformed. Since cortical recordings were generally lower in voltage relative to hippocampal recordings, these artifacts were more clearly present in mPFC LFPs. Therefore, mPFC LFPs were visualized and standard deviation thresholds were manually adjusted to capture large

voltage events. Once defined, the signals were then realigned to their corresponding session for later use (rat1 = 5std, rat2 = 3std, rat3 = no std cutoff required, rat4 = 3std, rat5 = 5std, rat6 = std). Next, the 5-100Hz filtered signals used for visualization were further filtered for 6-9Hz theta via third degree butterworth filtering, then phase was estimated via hilbert transform. We then identified times when voltages exceeded their corresponding standard deviation cut-offs, and removed phase values surrounding those events across all signals (one theta cycles worth of data in both directions surrounding an artifact).

Only units with >50 spike-phase estimations during both high and low coherence states were included (Siapas et al., 2005). Using random sampling procedures and Rayleigh's test of non-uniformity on a hippocampal place-cell modulated by theta (data from Pastalkova et al., 2008; Cohen, 2017), we confirmed that 97% of randomly sampled spike-phase distributions at 50 spike counts were significantly modulated by theta. This criterion was important to consider because there existed differences in the numbers of high and low coherence events. Rayleigh's test of non-uniformity was performed and a corresponding p-value was assigned to each neuron representing significant entrainment (*circ_rtest.m*). Firing rates were calculated by extracting spiking activity during high and low coherence epochs, then normalizing by the total amount of time in consideration.

Behavioral quantification and recording

Behavior was recorded from the rat using two approaches; 1) using a mounted camera sampled at ~30 pixels/sec (Cheetah; Neuralynx) that detects LEDs on the recording headstage and 2) by sending TTL pulses to Cheetah when infrared beams were broken on the maze via MATLAB. Time spent to choice was estimated using TTL pulses from the central door opening and from choice point exit (as defined by the infrared beam controlling the closing of the choice point door behind the rat). Behavioral complexity was calculated using the integrated change in absolute angular velocity (IdPhi; code provided by D. Redish; Papale et al., 2012; Redish, 2016) using position data obtained from central door opening to choice point exit. Position data was smoothed using a gaussian weighted filter (*smoothdata.m*), then velocity in the x (dX) and y (dY) dimensions are obtained using a discrete time-adaptive windowing approach (Janabi-Sharifi et al., 2000). Phi is defined as the arctangent of dX and dY, and dPhi is calculated by applying the time-adaptive windowing methodology on the unwrapped Phi estimates. IdPhi is then defined as the integral over the |dPhi| scores. Thus, for each trial, there is one IdPhi score that represents the overall head-movement complexity of the rat. Distance traveled in delay was used to assess whether general mobility differed between experimental and control groups. Position data was extracted from the 1.25s interval before the choice point door opened (e.g. delay exit), and total distance traveled was defined as the summation across instantaneous distance, calculated according to the distance equation:

$$Distance\ Traveled\ = \sum_{i=1}^{k} \sqrt{(x_{i+1} - x_i)^2 + (y_{i+1} - y_i)^2}$$

Where i refers to each video tracking data point through point k, and x/y refer to cartesian coordinates obtained through video tracking. Distance traveled was then normalized across each session to be between 0 and 1, then sorted according to trial-type.

Optogenetics

A Doric laser was programmed with the Neuroscience studio software to pulse blue (450nm) or red (638nm) lights in a square wave pattern. To test if VMT stimulation could enhance theta synchrony, a variety of stimulation parameters were tested. Likewise, stimulation frequency varied slightly between rats (between 7-8Hz and 5-15mW power). Laser power was tested prior to stimulation and red/blue lasers were matched in terms of mW output. Each rat contributed 1 session of data with anywhere between 80 and 110 stimulation events. A stimulation event lasted 2s and then the laser was turned off for 2-6sec. Red and blue laser stimulations were randomly interleaved. Stimulating the VMT of 21-42 revealed mixed results and sometimes visual observations failed to reveal clear theta in the mPFC, despite clear power increases (**Extended Fig. 7A and 7B; Fig. 8**). Since 21-42 received 2 injections at a single rostro-caudal location in the thalamus, and because the distribution of thalamic fibers targeting the mPFC and hippocampus varies along the rostro-caudal extent of the nucleus reuniens (Dolleman-var Der Weel, 2019), it was probable that VMT stimulation of 21-42 caused sparse activation of thalamo-cortical projections. Therefore, for 21-42 only, k-means clustering (2 clusters separating mPFC 6-9Hz power over stimulation epochs) was used to separate data to when VMT stimulation produced high powered mPFC theta rhythms. This approach revealed highly consistent results with rat 21-43 in terms of heightened theta coherence at ~9Hz (**Fig. 8**).

Statistics

Each figure panel was considered an independent analysis, and when significant p-values were observed (e.g. $p<0.05$), they were corrected for multiple comparisons using Bonferroni's method (original p-value multiplied by the number of tests performed) or in some cases using the Benjamini Hochberg method for many comparisons (**Fig. 3H; Fig. 8; Extended Fig. 7;** code: *fdr_bh.m* by David Groppe). If significance was not observed, the raw p-value was reported. Details regarding statistical testing were reported in the figure captions with information regarding p-value adjustment. Normalized difference scores were defined as such:

$$NormDiff\ = \frac{X - Y}{X + Y}$$

Where X and Y refer to within subject datasets. Normalized difference scores were tested for significance via t-test against a 0-null. Statistical testing was performed in MATLAB and Rstudio.

EXTENDED FIGURES

EXTENDED FIGURE 1

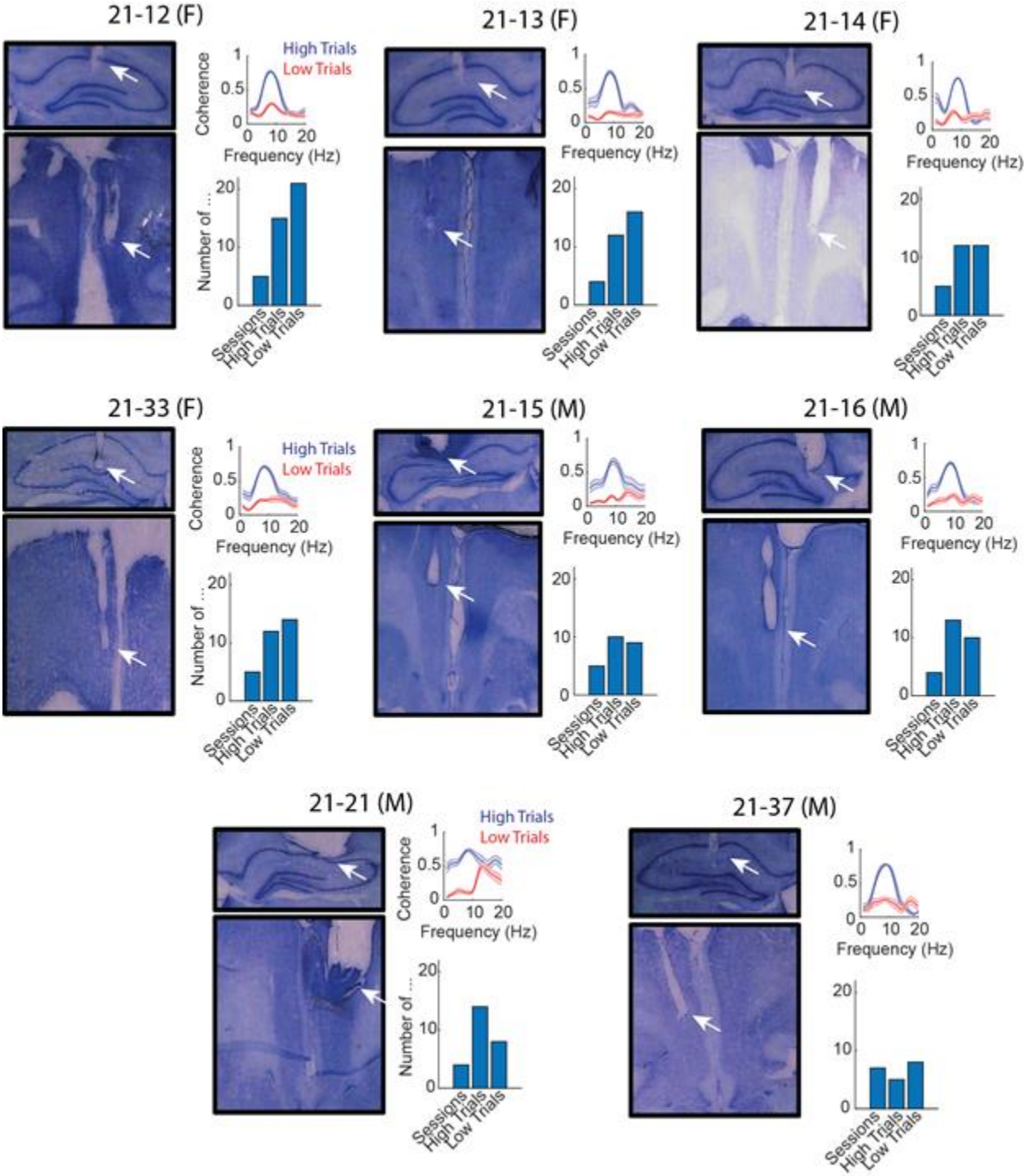

Extended Figure 1 | Histological verification from delayed alternation, brain machine interfacing rats. Per each subplot, the left panel shows histological verification of stainless steel wires targeting the mPFC and hippocampus. The right panels show coherence distributions on high coherence trials and low coherence trials,

as well as the number of sessions, and trial counts used to calculate choice outcomes following high or low coherence trial initiations. Notice that it took multiple sessions to achieve between 8 and 15 high and low coherence trials.

EXTENDED FIGURE 2

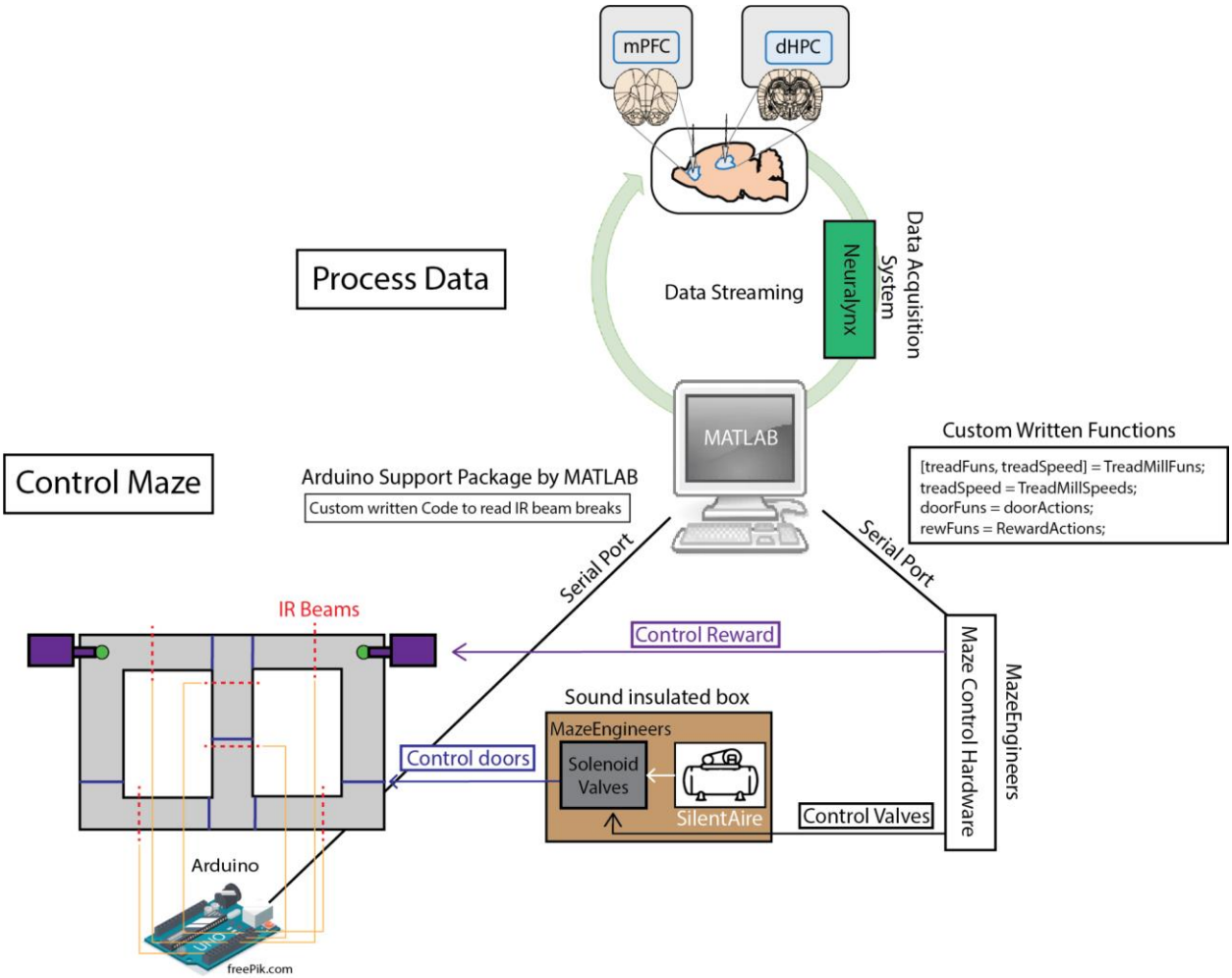

Extended Figure 2 | Two independent loops support brain machine interfacing. Schematic demonstration of how neural data could be processed in between control of the automatic T-maze. In terms of maze control, serial ports were formed between hardware built from MazeEngineers and an Arduino Uno board. Custom written functions were used to control solenoid valves, which pushed or released air, mediated by a silent air compressor. The solenoid valves and air compressor were placed in a large wooden box, with foam insulation walls, in order to reduce noise. The MazeEngineers hardware was also programmed to control the release of chocolate pellets for reward delivery. Using Arduino-powered infrared beam breaks (yellow lines denote connections), MATLAB could detect the exact location of the rat in order to carry out the programmed sequence of the task. For example, as rats approached a reward zone, an infrared beam break triggered the closing of a door (blue lines on maze) and the release of a reward (if a choice was correct).

EXTENDED FIGURE 3

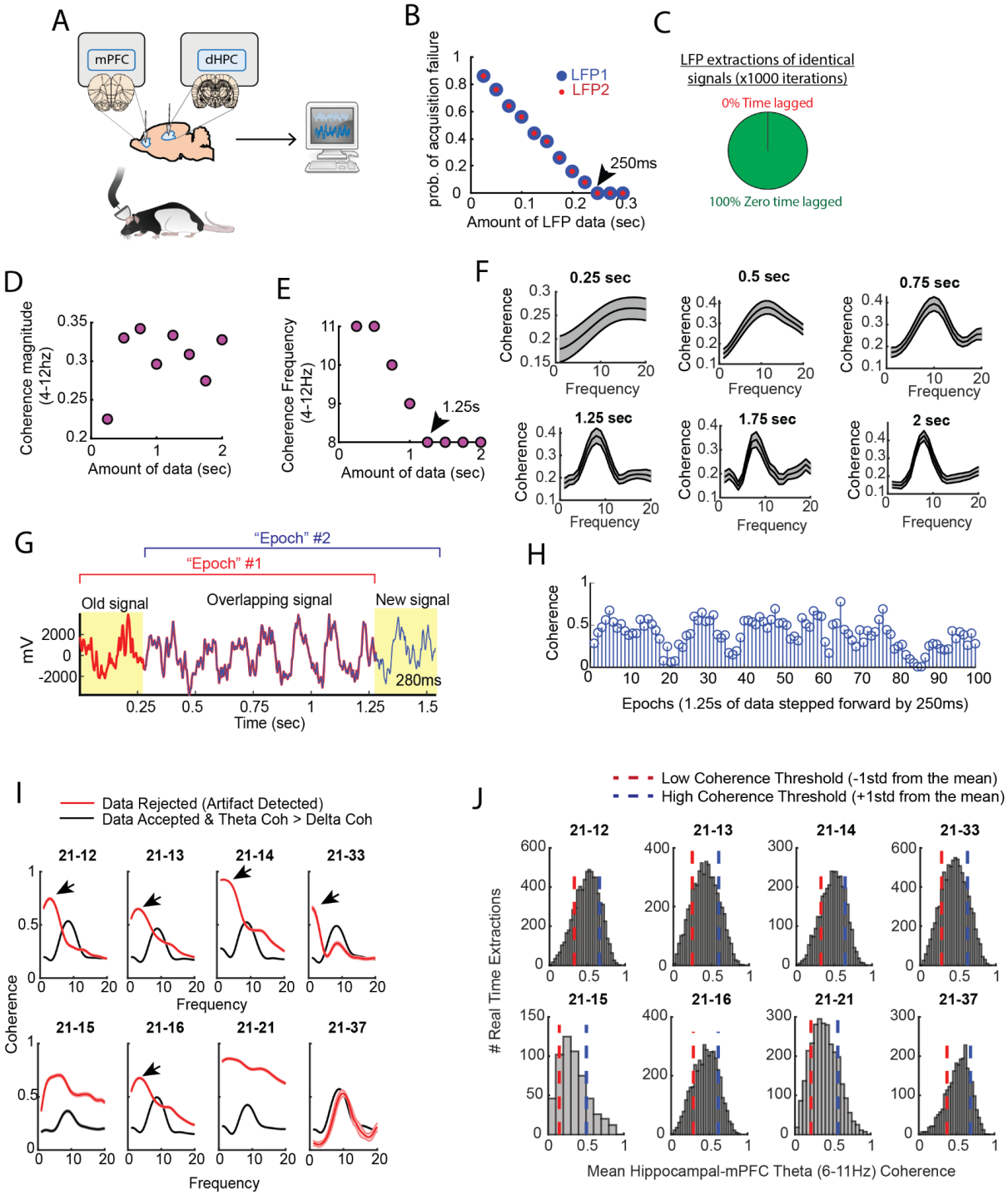

Extended Figure 3 | A) Cartoon schematic showing that signals were collected from the mPFC and hippocampus, then sent to a computer for processing in real-time. **B)** Two LFP signals were collected in real-time at various intervals, with an interval being defined as the time-lag in between attempted streaming from the acquisition system recording the neural data and the computer processing the data. Each data point represents an average from 50 attempted streaming events. Notice the negative relationship between the probability of streaming failure and the amount of data streamed. If our program waited 250ms in between streaming attempts, we found a 0 probability of acquisition failure. In practice, even at this interval, there were still rare acquisition failures that could be accounted for via programming. **C)** Two identical signals were programmed as two different recording channels in the DigitalLynx SX data acquisition system to test if serial streaming of two signals induced time-lags (e.g. one signal being temporally shifted in time relative to the other signal). We found that all serial streaming events were identical, indicating a zero time lag in between extracting two signals in real-time. **D)** Averaged coherence magnitude (4-12Hz) as a function of data size. Notice that at 250ms, coherence magnitude was highly underestimated. **E)** Coherence frequency (the frequency corresponding to the strongest coherence values) was modulated by the amount of data analyzed. Notice the coherence frequency to taper at 8Hz when analyzing at least 1.25s worth of data. **F)** Visual representation of the analyses shown in (**D and E)**. Notice that the shape of the coherence distributions vary as a function of the amount of data analyzed, but are generally consistent when analyzing at least 1.25s worth of data. **G)** A coherence “epoch” was defined as a 1.25s window, with each epoch varying by 250ms in time. The red colored signal was acquired first, the blue colored signal was acquired after 250ms, and the two signals were overlaid for visualization purposes. **H)** Stem plot showing theta coherence epochs as a function of time. Notice the rather smooth transitions between stronger and weaker theta coherence values, consistent with a moving window approach sharing a large proportion of data **(G)**. **I)** Real-time artifact rejection procedures contained strong delta coherence across all rats (red curves). When these artifact rejection procedures were combined with rejection of signals if delta coherence was stronger than theta coherence, highly consistent coherence distributions emerged (black curves). **J)** By performing these methods in real-time and gathering hundreds-to-thousands of theta coherence values (6-11Hz), coherence distributions were generated via offline data analysis. “High” and “low” magnitude theta coherence thresholds were then defined as +1std and -1std from the mean theta coherence value, respectively.

EXTENDED FIGURE 4

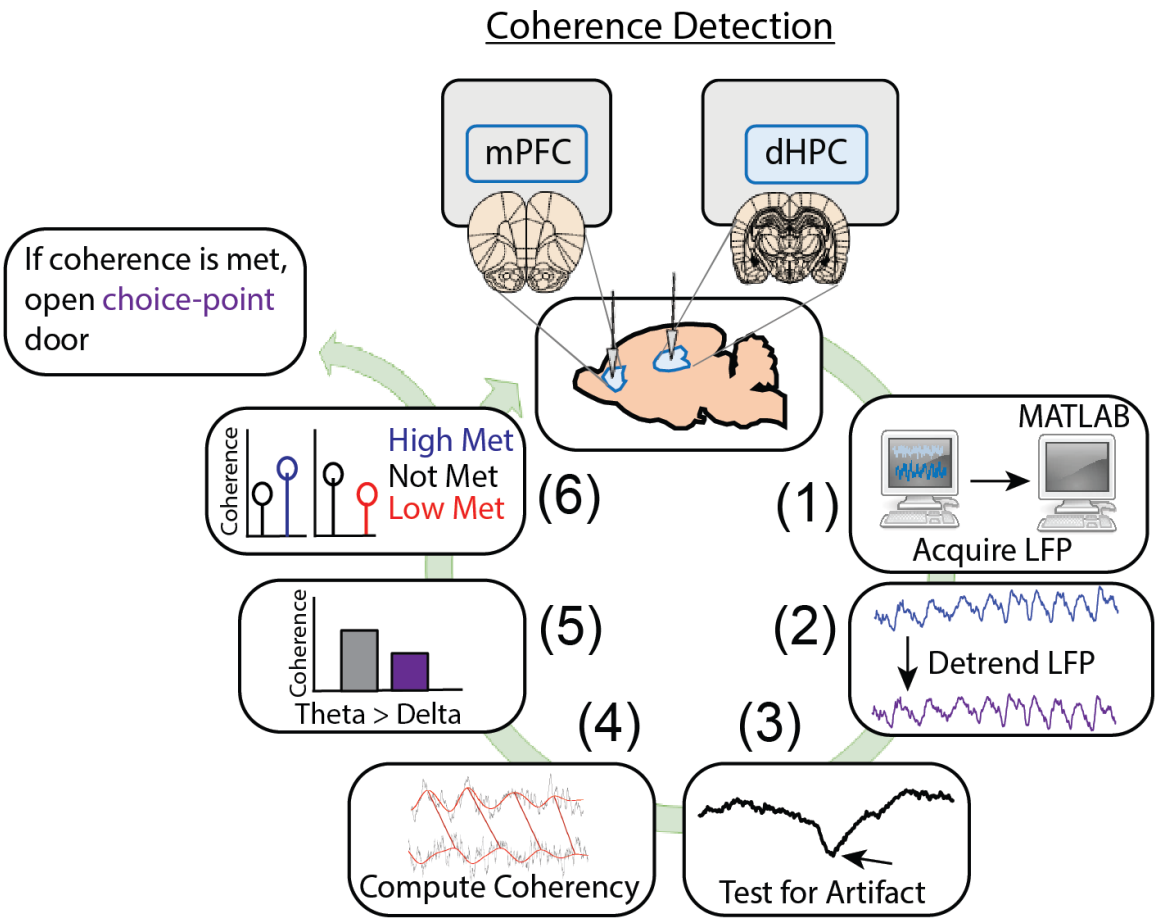

Extended Figure 4 | Detailed representation of brain machine interfacing. Data were acquired in real-time, then processed in MATLAB. Data processing consisted of fitting and removing a third degree polynomial to detrend the signals (1.25s worth of data), then signals were tested for artifacts. These artifacts were defined as large voltage fluctuations exceeding 4std of a mean and standard deviation generated from 10 minute baseline recordings (as rats occupied a flower pot with motion being more restricted than when on the maze). In real-time, if voltage fluctuations exceeded 4std and these events saturated >1% of the signal, then the brain machine interfacing restarted. If no artifacts were detected, coherence was calculated in 0.5Hz steps from 1-20Hz using *mscohere* and only if delta coherence (1-4Hz) exceeded theta coherence (6-11Hz), then brain machine interfacing restarted. If on a high coherence trial, theta coherence exceeded delta coherence, and theta coherence was higher than the

predetermined threshold, a door was opened, releasing the rat from being sequestered in the delay zone that separated trials. Upon release, rats could make a choice. Similarly, on low coherence trials, if the criterion described above was met and theta coherence was lower than the predetermined threshold, then the trial was initiated. If coherence was not met, the brain machine interface restarted.

EXTENDED FIGURE 5

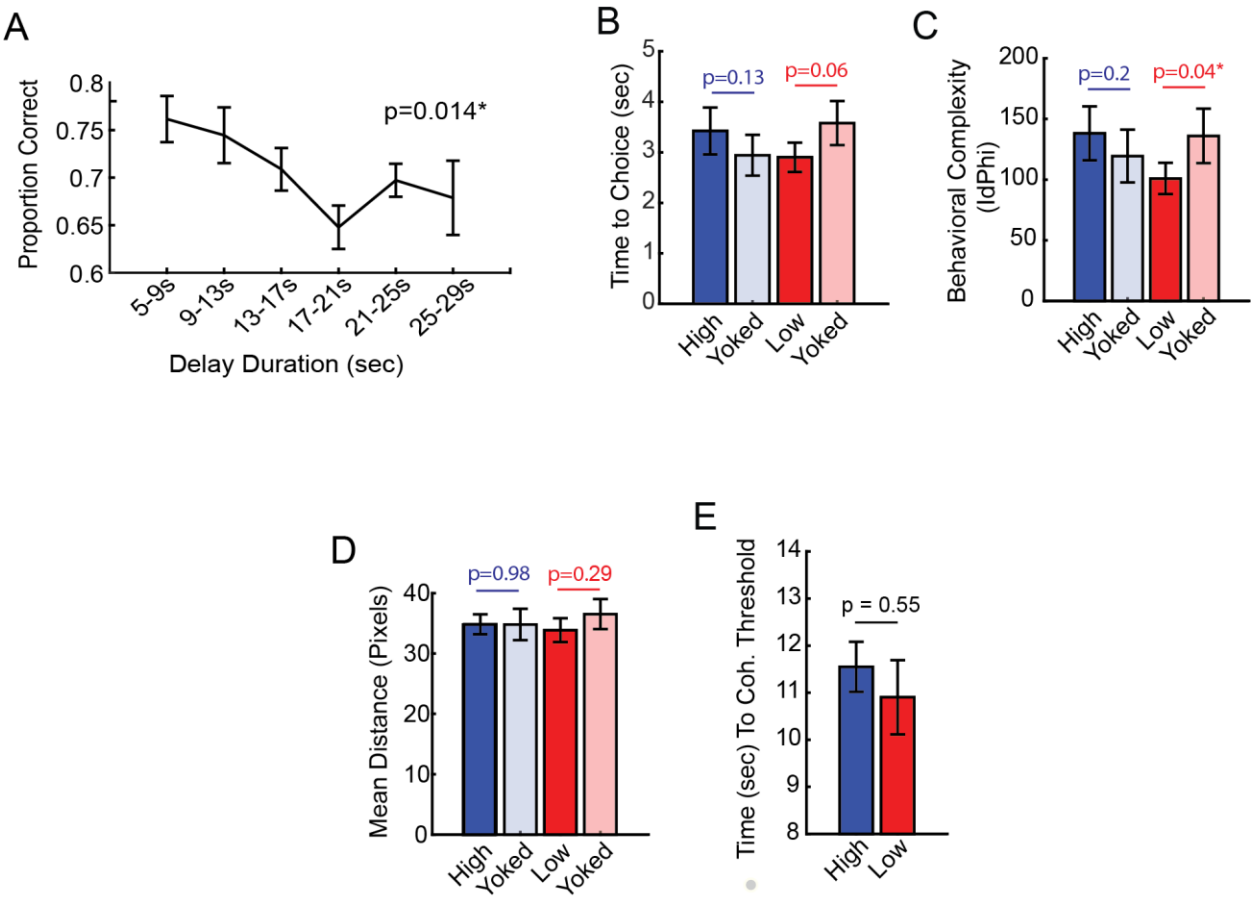

Extended Figure 5 | Follow-up behavioral analyses. A) During task training, time-spent in the delay zone was binned and the average proportion correct (# correct trials/ # trials) was calculated. There was a significant effect of delay duration on future choice outcomes (F(5,35) = 3.38; Repeated Measures ANOVA; N = 8 rats, 4 male, 4 female). This analysis validates the delayed alternation task being a working memory dependent task. **B)** Time to choice was calculated as the amount of time spent from trial initiation to choice exit (infrared beam break that triggers the reward release). There was no statistical difference between high and yoked trials, although there was a trending difference between low and yoked trials (t(7) = -2.23, ci = [-1.4 0.04]). **C)** Behavioral complexity (or head-movement complexity) was measured via the integrative change in

absolute angular velocity (IdPhi; Redish, 2016), a common metric to extract vicarious trial and error. Low coherence trials showed significantly lower IdPhi relative to yoked trials ($t(7) = -2.5$, ci = [-68.36 -1.9]). **D)** Distance (in pixels) was calculated in the last 1.25s before trial initiation, as these times were used to trigger trials according to theta coherence magnitude. There were no differences in distance traveled between coherence and yoked trials. **E)** The amount of time spent in the delay zone is a proxy of the amount of time it took to reach theta coherence thresholds. There was no significant difference in delay zone time-spent between high and low coherence trials. Planned comparisons between coherence and yoked trials were performed via paired t-tests. *$p<0.05$. P-values were shown in figure and the statistics were reported in the figure caption of $p<0.05$.

EXTENDED FIGURE 6

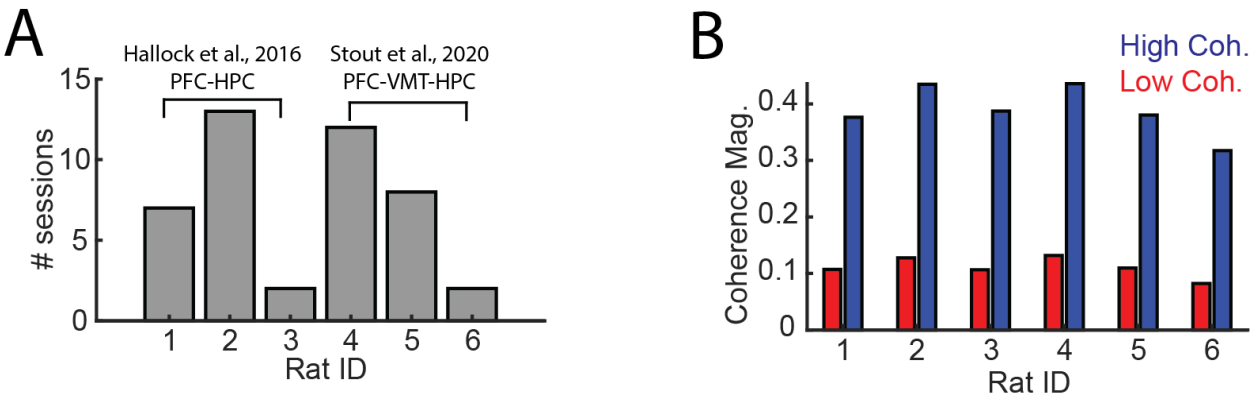

Extended Figure 6 | Details regarding mPFC-VMT-HPC recordings. A) Data from six rats were analyzed, three from Hallock et al., 2016 with simultaneous mPFC and hippocampal recordings and three from Stout and Griffin, 2020. **B)** High and low coherence thresholds were determined for each rat. Notice that thresholds were rather consistent across rats.

EXTENDED FIGURE 7

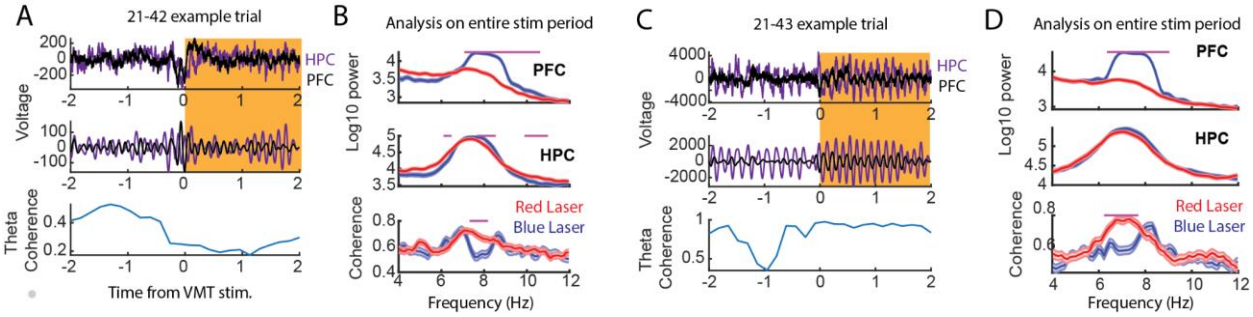

Extended Fig. 7 | The variable effects of VMT stimulation. A) Example stimulation epoch from 21-42. Notice that upon stimulation, theta coherence was dramatically reduced. **B)** When examining all stimulation epochs from 0-2s (yellow box in **A**; N = 64 blue laser stimulation events and 104 red laser stimulation events), we observed a clear reduction in mPFC-hippocampal theta coherence, despite increased mPFC and hippocampal theta power. **C)** An example stimulation epoch from 21-43. Note there was little impact on theta coherence from this epoch, however, notice the negative voltage deflection that occurred with stimulation. **D)** When collapsing all stimulation epochs from 0-2s (N = 113 blue laser stimulation events and 101 red laser stimulation events), we again observed a reduction in mPFC-hippocampal theta coherence. Compare these data to **Fig. 8**. Focusing on the 0.5-1.5s epoch following VMT stimulation increased mPFC-hippocampal theta coherence. These data show that VMT stimulation leads to variable consequences on synchronizing brain rhythms.